Progress in Additive Manufacturing
https://doi.org/10.1007/s40964-025-01457-y

RESEARCH

Design guidelines for laser powder bed fusion of triply periodic minimal surface structures for applications in smart reactors

Serhan Acikgöz[1] · Christoph Wigger[2] · Timo Merbach[2] · Felix Kexel[2] · Maria Isabelle Maiwald[1] · Dirk Herzog[1,3] · Ingomar Kelbassa[1,3] · Michael Schlüter[2]

Received: 9 July 2025 / Accepted: 28 November 2025

Abstract
Additive Manufacturing (AM), particularly Laser Powder Bed Fusion (PBF-LB/M), has transformed the production of complex metallic structures, enabling applications in smart reactors where enhanced heat and mass transfer at minimal pressure drop are critical. Triply Periodic Minimal Surface (TPMS) structures, such as Gyroid-TPSf and Schwarz-Diamond-TPSf geometries, offer unique advantages due to their high surface area-to-volume ratios, tunable porosity, and zero mean curvature. However, their manufacturability using PBF-LB/M remains underexplored, especially for demanding applications in process engineering that require structural integrity under extreme conditions. This study investigates the design and manufacturability of TPMS structures using 316L stainless steel via PBF-LB/M, focusing on the interaction of the key parameters porosity, unit cell size, and sheet thickness, of which two are independent variables while the third is a dependent variable. Through numerical simulations, experimental validation, and process optimization, practical design guidelines are developed. In this study, the design parameters of Gyroid-TPSf and Schwarz-Diamond-TPSf samples include porosities ranging from 70 to 90% and unit cell sizes from 2 to 20 mm. The results indicate that specifically, at large unit cell sizes (e.g., 20 mm), the decreased curvature radius reduces self-supporting effects, leading to insufficient mechanical stability during printing and resulting in local deformation. Conversely, at small unit cell sizes combined with high porosity levels (e.g., 2 mm and 90%), the sheet thickness becomes critically thin, often below the printable resolution, resulting in incomplete or fragile structures. CFD simulations were validated against experimental data across various volume flow rates. This work enables a knowledge-based selection of a suitable type of TPMS and its design parameters depending on the required flow characteristics in a given process engineering task while maintaining manufacturability. In conclusion, the study underscores the need for further refinement of design and manufacturing processes to fully exploit their benefits.

Keywords Additive manufacturing (AM) · Laser powder bed fusion (PBF-LB/M) · Triply periodic minimal surface (TPMS) · Smart reactors · Design guidelines

✉ Serhan Acikgöz
Serhan.acikgoez@tuhh.de

Christoph Wigger
christoph.wigger@tuhh.de

Timo Merbach
timo.merbach@tuhh.de

Felix Kexel
felix.kexel@tuhh.de

Maria Isabelle Maiwald
maria.maiwald@tuhh.de

Dirk Herzog
dirk.herzog@tuhh.de

Ingomar Kelbassa
ingomar.kelbassa@tuhh.de

Michael Schlüter
michael.schlueter@tuhh.de

[1] Institute for Industrialization of Smart Materials, Hamburg University of Technology, Hamburg, Germany

[2] Institute of Multiphase Flows, Hamburg University of Technology, Hamburg, Germany

[3] Fraunhofer Research Institution for Additive Manufacturing Technologies IAPT, Hamburg, Germany

Published online: 20 January 2026

Abbreviations

AM	Additive manufacturing
AMLS	Additively manufactured lattice structures
CFD	Computational fluid dynamics
HMI	Human–machine interface
PBF-LB/M	Powder bed fusion by laser beam/metals
POCS	Periodic open cellular structures
TPMS	Triply periodic minimal surface
TPnS	Triply periodic endo-skeleton
TPxS	Triply periodic exo-skeleton
TPSf	Triply periodic surface
UCS	Unit cell size

1 Introduction

Additive Manufacturing (AM) has transformed the manufacturing industry by enabling the production of complex geometries through a layer-by-layer material addition process. This innovative approach has unlocked new possibilities, particularly in applications where traditional manufacturing techniques struggle to meet complex design requirements. Among the various AM techniques, Laser Powder Bed Fusion (PBF-LB/M), as defined in DIN EN ISO/ASTM 52900:2022-03 [1], has emerged as one of the most promising for fabricating metallic components. Its ability to achieve high precision and accommodate complex geometries makes it essential in industries such as aerospace, biomedical engineering, and chemical processing [2].

In recent years, there has been growing interest in Triply Periodic Minimal Surface (TPMS) structures, which represent a unique class of geometries characterized by their zero mean curvature and periodicity in three dimensions [3, 4]. These structures are highly efficient in applications requiring optimized mass and heat transfer due to their high surface area-to-volume ratios and tunable porosity [5, 6]. Regular structures, such as those found in TPMS, can be produced through additive manufacturing and are often referred to as Additively Manufactured Lattice Structures (AMLS). Examples of practical applications include heat exchangers, filtration systems, and chemical reactors [7].

With the increasing demand for advanced materials capable of performing in extreme operating environments, particularly in process engineering applications, there is an urgent need to develop a systematic approach for optimizing the design and manufacturing of TPMS structures. The next generation of reactors for process engineering require materials and structures that can endure high mechanical and thermal stresses while simultaneously improving process efficiency through enhanced heat and mass transfer. TPMS structures are ideally suited for these applications due to their unique geometric properties [8–10].

While extensive literature exists regarding the AM and mechanical characterization of TPMS [8, 11–13], the research presented here aims at informing process engineers about the performance, i.e. pressure loss, specific surface area, and heat transfer, as well as the printability of two selected TPMS types in dependence of porosity and unit cell size. By integrating numerical simulations, experimental validation, and process optimization, this study establishes application-specific practical design guidelines. These guidelines not only support the implementation of TPMS structures in real-world engineering systems but also pave the way for their widespread adoption in demanding applications such as SMART reactors, i.e. reactors which can convert sustainable renewable resources into different products (multi-purpose) in a more sustainable way and operate autonomously (self-adapting), leading to more resilient processes that are more transferable between scales and locations [14].

2 State of the art

While PBF-LB/M offers unmatched precision and design flexibility, it is not without its challenges. The precision of the laser beam and the behavior of the powder set limits on the minimum feature sizes that can be reliably printed. Additionally, the rapid heating and cooling cycles inherent in the process create significant thermal gradients, leading to residual stresses that can cause warping or cracking of the part. Moreover, the interaction of multiple process variables, such as laser power, scan speed, and powder characteristics, requires careful optimization to achieve consistent results [15, 16]. To address these challenges, several design guidelines have been developed to optimize manufacturability, particularly for conventional materials such as stainless steel [17], titanium [18], and nickel-based superalloys [19].

Kranz et al. [18], for instance, focused on the manufacturability of Ti–6Al–4V and emphasized the importance of geometric constraints for achieving reliable thin-walled features, beam elements, and boreholes. The study highlights the critical role of wall thickness in ensuring structural integrity, recommending a minimum of 0.5 mm for thin walls to prevent distortions during the cooling phase. Kranz et al. [18] also analyzed support elements, demonstrating the need to define minimum thicknesses to reduce excessive deformation, and provided strategies for optimizing support structures by strategically placing these elements to minimize material consumption while maintaining part quality.

Herzog et al. [19] extended these guidelines to Inconel 718, a high-performance superalloy used in aerospace and energy applications. A minimum thickness of 0.3 mm for small freestanding walls and 0.6 mm for larger walls is

suggested, ensuring that structures can reach heights of up to 30 mm without deviation from design specifications. A critical overhang angle of at least 25° is defined and a recommendation is given that overhangs longer than 1.0 mm should be supported to prevent deformation. In addition, innovative design features such as tear drop shapes are introduced, which can eliminate the need for internal supports when the overhang angle exceeds 45°, and the use of lattice structures for weight savings and structural reinforcement is investigated.

Adam and Zimmer [17] highlight the importance of geometric constraints in design and propose comprehensive guidelines for optimizing design parameters using 316L stainless steel. The research outlines the critical role of wall thickness, recommending that the minimum thickness should be at least 1.5 times the layer thickness (t_L) to ensure sufficient structural stability. For the PBF-LB/M process, where the layer thickness is 0.030 mm, a minimum wall thickness of 0.6 mm is suggested. Adam and Zimmer [17] also established guidelines for cylindrical structures, stating that their diameters should not fall below 1.5 times the wall thickness to prevent deformations. This results in a recommended minimum cylinder diameter of 6 mm based on a wall thickness of 4 mm. In addition, their study addressed spacing between overhanging elements and recommended a minimum distance of twice the wall thickness to minimize the risk of part deformation while maintaining sufficient structural connections.

While these guidelines provide essential constraints for manufacturing bulk components, their direct applicability to complex cellular structures, such as TPMS geometries, remains limited. TPMS structures represent a class of geometries characterized by continuous, non-self-intersecting surfaces with periodicity in three dimensions [3]. Their defining feature is a zero mean curvature, which minimizes surface area for a given volume while maintaining high structural efficiency [3, 4, 12]. Among the most widely studied TPMS structures are the Gyroid and Schwarz-Diamond geometries, both of which exhibit exceptional mechanical and functional properties [20]. Due to their high surface-area-to-volume ratio, TPMS structures are particularly advantageous in applications requiring efficient mass and heat transfer, such as heat exchangers, filtration systems, and smart chemical reactors [5, 21]. Their inherent symmetry and periodicity allow for precise control over properties such as porosity, stiffness, and strength, making them highly adaptable to specific engineering requirements [22]. Mathematically, TPMS describes a surface with infinitesimal thickness. For realization of a TPMS in AM, it is possible to derive printable subtypes by considering either the surface with a sheet thickness within the manufacturing limits, or by considering the volumes between the surface. According to the nomenclature by Fisher et al. [4], TPMS structures can therefore be subdivided into surface structures (TPSf, i.e. the surface with a printable thickness is considered as the solid part of a TPMS unit cell), endo-skeleton (TPnS) and exo-skeleton structures (TPxS), with the latter representing the volume between the surfaces as solid part of the unit cell. The mathematical formulations for the Gyroid and Schwarz-Diamond structures are detailed in the works of Reynolds et al. [23] and Lu et al. [24].

Jones [13] investigated the manufacturability of TPMS structures using PBF-LB/M with AlSi10Mg and identified key design guidelines to minimize defects and improve geometric accuracy. The study found that inclination angle is the most critical factor for manufacturing quality. Specifically, angles below 30° result in significantly increased surface roughness ($Ra > 40$ µm) and geometric deviations. In contrast, structures with an inclination angle of at least 50° showed significantly lower roughness. Local curvature also affects manufacturability. Flat or nearly flat regions with low curvature (< 2500 m^{-2}) are particularly sensitive to defects such as layer delamination or surface distortion. In contrast, highly curved geometries (> 2500 m^{-2}) showed better dimensional accuracy and reduced defect formation. Based on these findings, Jones [13] developed an analytical model to predict manufacturing defects by integrating inclination angle, curvature, and wall thickness. The model demonstrates that TPMS structures such as gyroids are particularly advantageous for PBF-LB/M due to their inherent curvature and uniform inclination angle distribution. To support design optimization, the TPMS Designer software tool was developed. This tool enables parametric generation and analysis of TPMS geometries by calculating key parameters such as curvature, inclination angle, and volume fraction. It helps identify potential problem areas during the design phase and allows for early design adjustments.

While some studies have explored the manufacturability of TPMS structures via PBF-LB/M, these investigations have largely focused on aluminum alloys, as demonstrated in the work of Jones [13]. However, there is a lack of comprehensive studies addressing the manufacturability of TPMS structures in stainless steel 316L, which is of particular interest due to its corrosion resistance and high mechanical performance [25].

Recent work by Qu et al. [8] provides first material-specific guidelines for PBF-LB/M of TPMS structures in stainless steel 316L. In this work, the optimal parameters for fabricating thin-walled structures using micro PBF-LB/M are systematically explored using cubes and thin-walled samples by adjusting laser power, scanning speed, and hatch distance. The study investigates relative density, surface quality, thin-wall process limitations, and dimensional accuracy of components. It was found that the wall thickness

of thin TPMS structures should be at least 200 µm to prevent deformation and fractures, with progressive reductions down to around 100 µm being achievable through optimized process conditions. Using these optimized parameters (e.g., moderate laser power ~ 50 W, scanning speed ~ 1000 mm/s, hatch distance ~ 0.03 mm, and energy density ~ 100 J/mm^3), thin-walled TPMS structures can achieve high relative density (> 99.7%) and smooth surfaces (Ra ≈ 2 µm). Moreover, these thin-walled TPMS lattices exhibit enhanced heat dissipation, underlining their functional potential beyond lightweighting.

However, the limited scalability of the micro PBF-LB/M process highlights the need for further research. The design limits and correlations established for micro PBF-LB/M cannot be transferred directly to the macro scale due to differences in feature resolution, melt pool dynamics and process stability. Furthermore, the effect of different TPMS types and parameters on standard performance metrics in process engineering, such as pressure drop, specific surface area and heat transfer efficiency, remains insufficiently understood.

Existing research has provided valuable insights into fundamental design guidelines for PBF-LB/M, primarily focusing on conventional materials and bulk geometries, and a number of studies have focused on PBF-LB/M of TPMS structures and their mechanical characterization. For application in process engineering, this paper seeks to enhance the State of the Art by

- assessing the printability of TPSf structures for defined porosity and unit cell size combinations relevant for applications in process engineering,
- clarifying failure modes in printing of TPSf leading to loss of structural integrity,
- proposing a new methodology to assess structural integrity of the build TPSf structure by overlay of profilometer data with CAD-data, to allow for an unbiased qualitative assessment,
- and correlating manufacturable porosity and unit cell size combinations to relevant performance values in process engineering, such as pressure drop and heat transfer.

3 Methodology

3.1 Selection of TPMS structures

The selection process of TPMS structures for a given application focuses on identifying geometries that combine functional effectiveness with manufacturability. Two prominent structures, the Gyroid-TPSf and Schwarz-Diamond-TPSf, are chosen for detailed investigation due to their advantages in terms of mechanical properties and flow dynamics (for visualization of the structures see Fig. 3) [6, 20]. Both structures exhibit excellent heat and mass transfer capabilities, making them suitable for applications such as heat exchangers and chemical reactors.

For the experimental work, 316L stainless steel is selected as the base material due to its corrosion resistance, mechanical robustness and compatibility with the PBF-LB/M process. The 316L stainless steel powder, supplied by *SLM Solutions (Lübeck, Germany)*, complies with the DIN EN 10088 standard. The powder's spherical particle morphology, with a size distribution between 10 and 45 µm, ensures optimal flowability and uniformity during the powder bed fusion process [25].

3.2 Experimental design

In process engineering applications, TPMS structures are regularly optimized to achieve maximum heat and mass transfer efficiency at minimal pressure drop, and high manufacturability. These structures inherently have three primary design parameters: porosity (ε), unit cell size (ucs), and sheet thickness (t_s). However, only two of these parameters can be chosen independently, while the third is derived from the selected values. Porosity primarily determines the surface-to-volume ratio for catalytic reactions. The unit cell size and sheet thickness directly influence the mechanical stability of the structure as well as the pressure drop across it. In this study, porosity and unit cell size are varied since these are typical design parameters of periodic open cellular structures (POCS) used in process engineering, while the resulting sheet thickness is determined accordingly. Porosity is defined as

$$\varepsilon = 1 - \frac{V_{struts}}{V_{solid}} \tag{1}$$

where V_{struts} is the volume of the solid struts forming the lattice structure and V_{solid} is the volume of the bounding box [26]. In TPMS, V_{struts} is represented as the volume defined by the surface of the TPMS and the sheet thickness according to Eq. (1). The influence of these design parameters on specific surface area, pressure drop and heat transfer is later discussed in Section 5.

The design and optimization of Gyroid-TPSf and Schwarz-Diamond-TPSf structures is conducted using *nTopology (New York, USA)*, a specialized software platform for advanced geometric modeling and simulation. Each sample is designed with an external rectangular frame, measuring 20 × 20 × 21 mm^3 (L × W × H). These dimensions are chosen to standardize the geometry for comparative analysis. The

Table 1 Design parameters of Gyroid-TPSf and Schwarz-Diamond-TPSf samples: target porosity ε_t, unit cell size ucs and resulting target sheet thickness $t_{s,t}$

Type		Gyroid-TPSf				Schwarz-Diamond-TPSf			
ε_t	[%]	70							
ucs	[mm]	2	5	10	20	2	5	10	20
$t_{s,t}$	[mm]	0.196	0.490	0.980	1.960	0.160	0.400	0.800	1.600
ε_t	[%]	80							
ucs	[mm]	2	5	10	20	2	5	10	20
$t_{s,t}$	[mm]	0.132	0.330	0.660	1.320	0.104	0.260	0.520	1.040
ε_t	[%]	90							
ucs	[mm]	2	5	10	20	2	5	10	20
$t_{s,t}$	[mm]	0.064	0.160	0.320	0.640	0.052	0.130	0.260	0.520

Table 2 Overview of process parameters for standard and adapted settings

Parameter	Unit	Values	
		Standard	Adapted
Slicing	–	Enable point reduction	No point reduction
Hatching, in skin	–		
· Borders: Beam Compensation	mm	0.10	0
· Hatch Offset	mm	0.08	0
· Hatch Distance	mm	0.08	0.10
· Pattern style	–	No pattern: Zig-Zag (unconnected)	Offset filling: Out to in

additional height of 1 mm was specifically included to facilitate the removal from the build plate without compromising the integrity of the structural features. Since the objective is to provide practical information on which combinations of ε and ucs are printable and in which geometrical tolerance, ε and ucs are varied and the resulting target sheet thickness is determined, as shown in Table 1. To derive the target sheet thickness, it was iteratively changed until the desired porosity at a given ucs was met. Due to heat conduction, the melt pool diameter typically exceeds the laser beam diameter [27], thus limiting the expected minimum realizable sheet thickness. Therefore, the parameter window of ε-ucs-combinations is limited to values that result in target sheet thicknesses above or in the region of the focal diameter, to avoid builds that are physically impossible to build and to still capture the manufacturing constraint, i.e. the minimum realizable sheet thickness of the respective TPSf structures.

The TPMS are manufactured using a *TruPrint1000 (Trumpf Se+Co. KG, Ditzingen, Germany)* PBF-LB/M system equipped with a 200 W laser and a comparatively small focal diameter of 55 µm. The production of the TPMS structures using the *TruPrint1000* highlighted the need for precise control of the process parameters to achieve optimum results, as the parameter set needed adaptation to enable printing of thin wall thicknesses below 0.25 mm. Structures with sheet thicknesses below 0.25 mm tend to fail due to incorrect slicing or missing layer information. This phenomenon is also observed when using the adapted parameter set, despite the fact that this set enables printing at reduced layer thicknesses. The details of these process parameters, both standard and adapted, are summarized in Table 2, while the differences between them during slicing are illustrated in Fig. 1.

Figure 1 shows the calculated exposure paths for the standard and adapted process strategies as displayed in the Human–Machine Interface (HMI) of the *TruPrint1000*, which is used for build job preparation and slice preview. Using the standard settings, discontinuities can be observed in the contour and hatching paths. Especially for very fine structures (ucs = 2 mm) or high porosity (ε = 90%), certain exposure paths are missing, leading to incomplete or interrupted melting tracks. With the adapted settings, continuous and complete exposure paths are generated. Both contours and infills are consistently exposed.

After the print, the remaining powder was removed through air blasting and the parts were detached from the build platform using wire Electrical Discharge Machining for further evaluation without any heat treatment.

3.3 Evaluation methods

For applications in process engineering, two main requirements exist. First, the build TPMS needs to maintain structural integrity, i.e. no defects resulting in 'open' connections between the two channels of a Gyroid-TPSf are allowed, as this would impact flow, mixing etc. Second, the actual porosity should not deviate from the target porosity. This aspect is clearly linked to the actual sheet thickness, which will impact the actual porosity of the build structure. Close to the manufacturing limits, where deviations are unavoidable, it is desirable to know the correlation between actual and target porosity so it can be considered already in the design stage.

Target porosity values are calculated using the formula embedded in *nTopology*. To check these target values, the printed samples are weighed using a scale and the actual

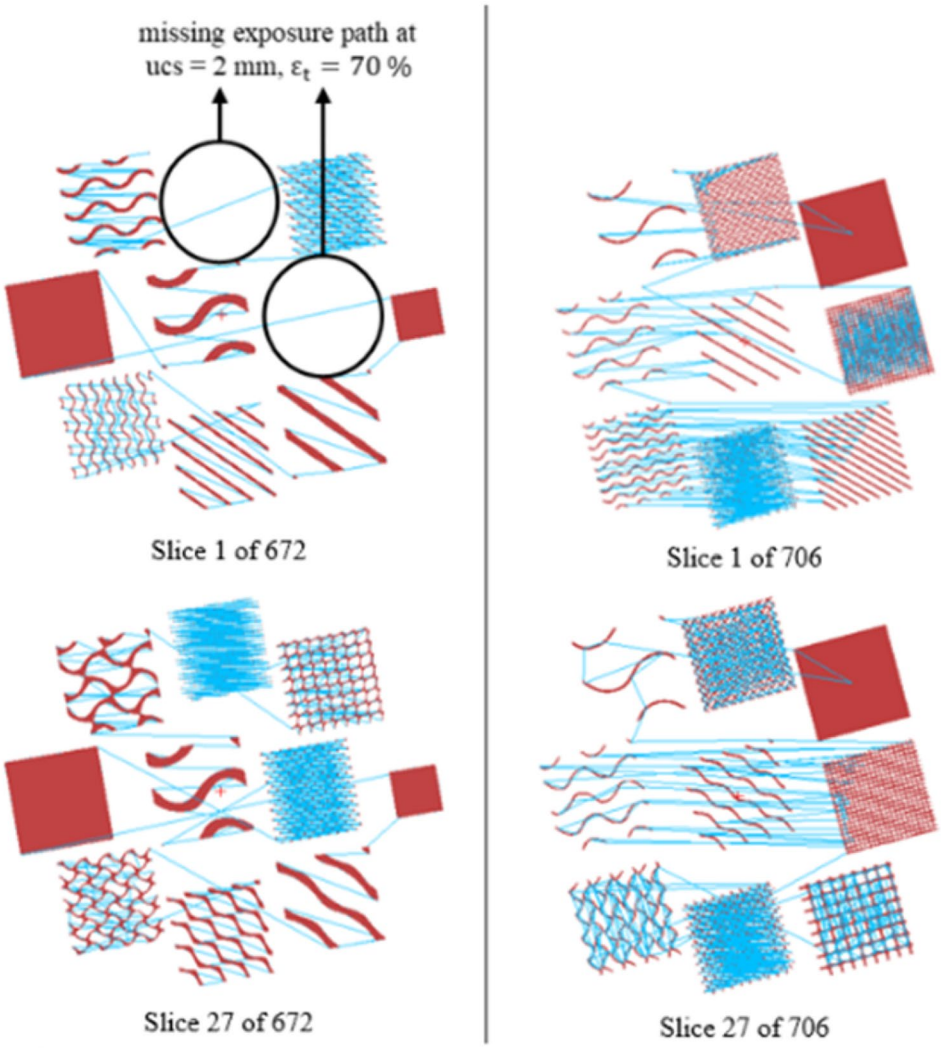

Fig. 1 Exemplary slicing results, showing contour path with standard (left) and adapted settings (right)

porosity is determined. A comparison is then made between the target values and the actual porosity values.

The actual sheet thickness is analyzed using a high-precision profilometer *(Keyence VR-6000, Neu-Isenburg, Germany)*, which provides detailed measurements of surface geometry and thickness variations of the TPMS structures. The measurements focus on validating the designed thickness ranges (0.052 mm to 1.96 mm) and are conducted specifically at the outer boundary of the unit cell size, where the sheet thickness is oriented perpendicular to the observation plane. Additionally, sheet thickness was evaluated at different locations on selected samples, yielding values with insignificant variation (i.e., below 5 µm), indicating uniformity across the structures.

To evaluate the structural integrity of the printed Gyroid-TPSf and Schwarz-Diamond-TPSf components, surface measurements of the manufactured structures are taken using a high-precision profilometer. These measurements are compared to the surfaces of the original designs created in *nTopology*. The evaluation process involves overlaying the measured surface profiles with the corresponding digital models to identify discrepancies and damaged areas within the printed structures (also refer to Sect. 4.3 and Fig. 4).

4 Results and discussion

The presented results underline the influence of design parameters and process settings for both Gyroid-TPSf and Schwarz-Diamond-TPSf.

4.1 Deviation of porosity

The relationship between the unit cell size and the deviation of porosity ($\Delta\varepsilon$) for both Gyroid-TPSf and Schwarz-Diamond-TPSf structures is shown in Fig. 2. To quantify $\Delta\varepsilon$, the measured porosity of each sample is compared to its respective target porosity. The porosity deviation, $\Delta\varepsilon$, is taken as the absolute deviation, defined by the difference

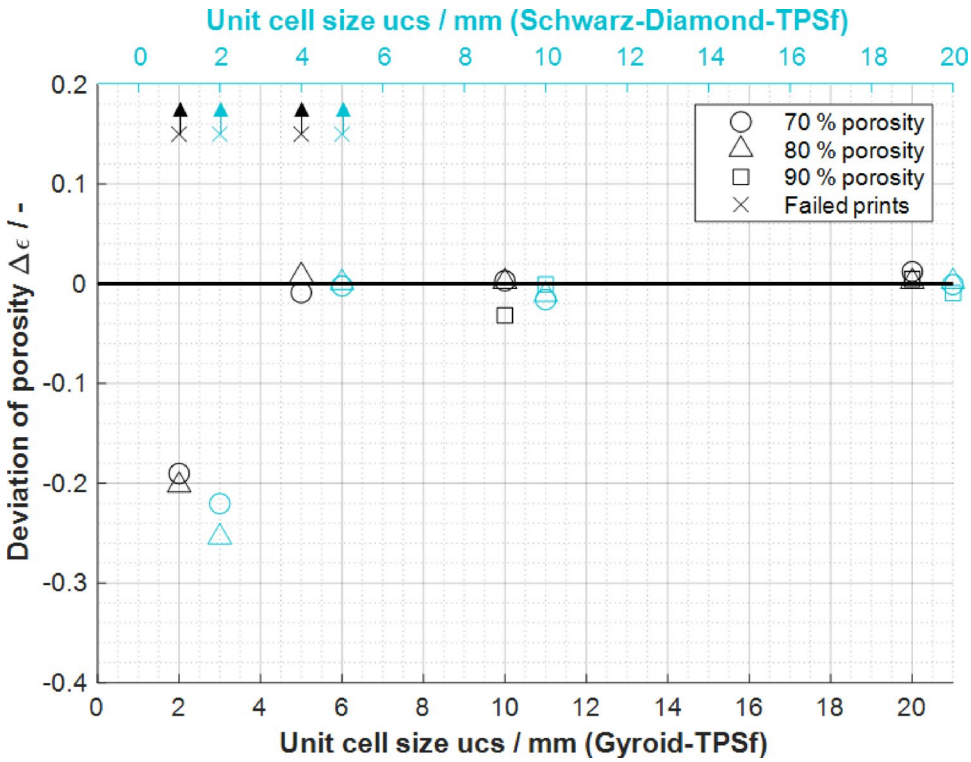

Fig. 2 Deviation of porosity as a function of unit cell size for Gyroid-TPSf (black) and Schwarz-Diamond-TPSf (light blue) structures at target porosities of 70%, 80% and 90%. Please note that the scale for the Schwarz-Diamond-TPSf is shifted to avoid overlap of data points

between the measured porosity and the target porosity. This is expressed as

$$\Delta\varepsilon = \varepsilon_m - \varepsilon_t \tag{2}$$

where ε_m represents the actual porosity determined from experimental measurements, and ε_t is the target porosity value defined in the design phase. The diagram illustrates how $\Delta\varepsilon$ varies as a function of unit cell size for both structure types, ranging from 2 to 20 mm. These results provide insights into how geometric parameters influence the accuracy of porosity reproduction, highlighting deviations that arise due to manufacturing constraints and process-related effects.

For the Gyroid-TPSf structures, it is observed that a smaller unit cell size of 2 mm leads to significant deviation of porosity. The data points for these porosities indicate negative deviations, with $\Delta\varepsilon$ reaching values below − 0.2. This significant deviation can be attributed to the limited precision of the manufacturing process under the investigated conditions and parameters when dealing with fine geometries, as the actual geometry suffers from overmelting. The deviation becomes minimal at ucs = 5 mm and remains consistent at ucs = 10 mm for 70% and 80% porosity. For 90% porosity at ucs = 10 mm, a slight negative deviation is observed due to the reduced sheet thickness at high porosities. At ucs = 20 mm, the deviation is once again negligible, showing that the process can reproduce the target porosity.

Similar to Gyroid-TPSf, the Schwarz-Diamond-TPSf structures show a higher deviation of porosity for small unit cell sizes, particularly at 2 mm. At this scale, the deviation for 70% and 80% porosity exceeds almost − 0.25, which is even higher than that observed in Gyroid-TPSf structures. This highlights the increased complexity of accurately manufacturing Schwarz-Diamond geometries at smaller scales. As the unit cell size increases, the deviation for all porosity levels decreases and approaches zero. The accuracy is already very high at ucs = 5 mm and remains stable at ucs = 10 mm across all porosity levels, with minor variations due to reduced sheet thickness at higher porosities. At ucs = 20 mm, the deviation is again minimal.

Considering that the porosity deviation increases with higher target porosities and smaller unit cell sizes for both geometries, it is assumed that this might be caused by the limited capability of the process to manufacture the associated, increasingly thin sheet thicknesses. Therefore, in the next section the actual sheet thickness will be examined to link the design parameters to the manufacturability outcomes.

4.2 Sheet thickness

Based on the analysis of porosity deviations, the measured sheet thickness ($t_{s,m}$) is now evaluated in relation to the target sheet thickness ($t_{s,t}$) for both Gyroid-TPSf and Schwarz-Diamond-TPSf structures.

The relationship between $t_{s,t}$ and $t_{s,m}$ for Gyroid-TPSf and Schwarz-Diamond-TPSf structures is presented in Fig. 3. The diagram illustrates the influence of porosity (70%, 80%, and 90%) and manufacturing parameters (standard vs. adapted) on the fabricated sheet thickness. The differences between the standard and adapted parameters are already listed in Table 2.

The dashed lines represent the tolerance band based on the IT10 tolerance class with an allowed deviation of ± 0.04 mm, which is used as a reference. The results show that both Gyroid-TPSf and Schwarz-Diamond-TPSf structures with a small unit cell size of 2 mm and porosities of 70% and 80% do not fulfill IT10. This is attributed to the focal diameter of 55 µm on the TruPrint1000, which makes it challenging to precisely reproduce sheet thicknesses below 0.25 mm.

The results support the hypothesis that the previously found deviations in porosity can be attributed to deviations in actual sheet thickness. The analysis demonstrates that an increase in target sheet thickness improves the dimensional accuracy of both Gyroid-TPSf and Schwarz-Diamond-TPSf structures. As the unit cell size and corresponding target sheet thickness increase, the measured sheet thickness approaches the target value ($t_{s,t}$). Furthermore, it can be concluded that accurate reproduction of the designed geometry in *nTopology* is ensured as long as sheet thicknesses below 250 µm are avoided. From a manufacturability stand point, this slightly favors the Gyroid-TPSf over the Schwarz-Diamond-TPSf due to slightly thicker resulting sheet thicknesses for same combinations of ε and ucs (cf. Table 1).

In general, increasing porosity or reducing unit cell size leads to reduced sheet thickness, which first causes geometrical deviations due to overmelting of the contour and, if further reduced, ultimately results in build failure.

4.3 Integrity of the structure

To evaluate the structural integrity of the printed Gyroid-TPSf and Schwarz-Diamond-TPSf structures, a direct comparison between the measured and designed surfaces is conducted. Structural integrity is here defined as the ability of the printed structure to maintain its designed geometry continuously, without critical defects or loss of connectivity, throughout the specified depth range. This approach allows for a detailed analysis of whether the fabricated structures maintain a continuous geometry without significant defects, as intended in the digital design. The high-precision profilometer captures the surface profile over a defined depth range of 1 mm. The depth range is shown in a colour scale in Fig. 4. The selection of this depth range is crucial to ensure that minor height variations due to surface roughness or powder adhesion are not mistakenly interpreted as structural defects. To enable a reliable comparison, the same depth setting is applied in *nTopology*, where a projection of the designed structure is generated. The criterion for structural integrity is explicitly defined as the continuous presence of the structure within the analyzed depth range, indicating that no critical voids or deformations compromise the mechanical stability of the lattice. Figure 4 presents an example of the proposed evaluation method applied to a Schwarz-Diamond-TPSf structure. The color-coded overlay

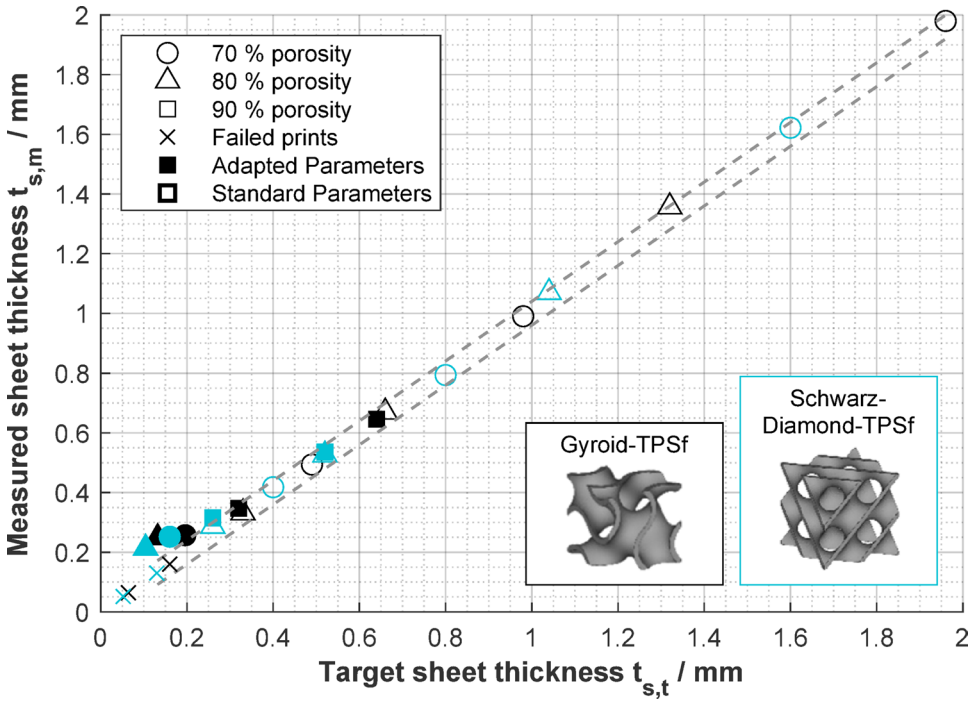

Fig. 3 Correlation between target and measured sheet thickness for Gyroid-TPSf (black) and Schwarz-Diamond-TPSf (light blue) structures at varying porosity levels and manufacturing parameters

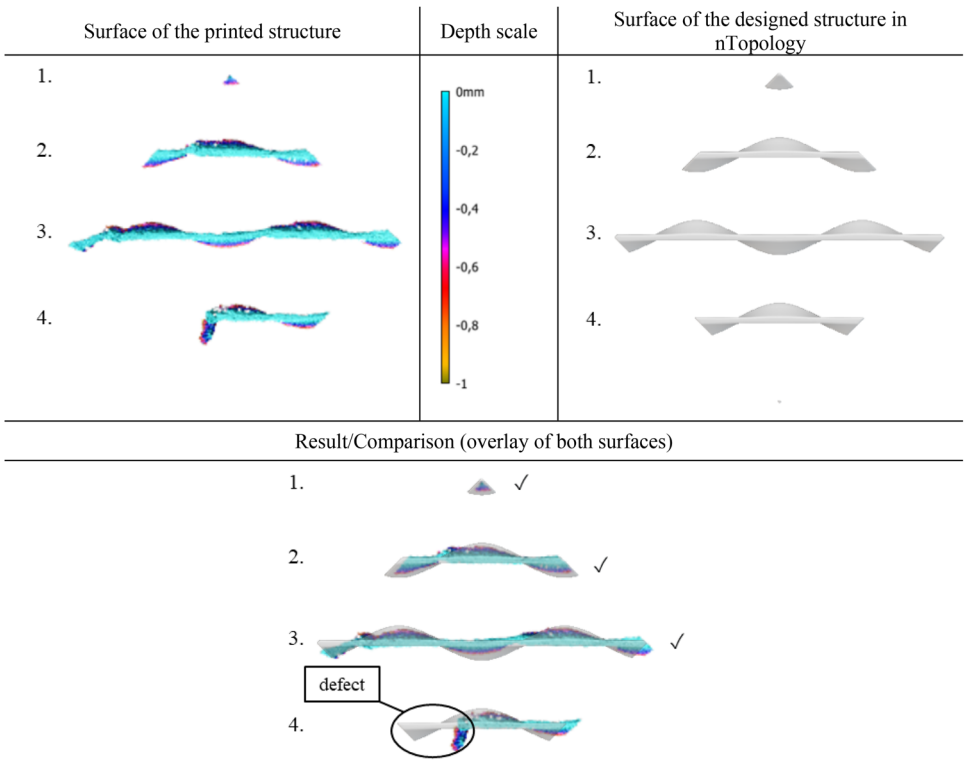

Fig. 4 Proposed methodology to evaluate the integrity of the printed TPMS structures, exemplarily shown for a Schwarz-Diamond-TPSf structure (ε = 90%, ucs = 20 mm)

highlights areas where the structure has been successfully fabricated, as well as regions where material is missing or significant deviations from the target geometry occur. To facilitate interpretation, critical defects are visually marked in the overlay in Fig. 4 to identify regions where the structure is incomplete or significantly deformed. Structurally intact areas, where the printed geometry closely matches the design, are marked with check symbols in Fig. 4 for clear identification. This graphical representation enhances the assessment of manufacturing quality and enables a precise identification of critical areas within the printed structures.

The evaluation of the Schwarz-Diamond-TPSf structures is shown in the following Figs. 5 and 6. At first, the results for very small unit cell sizes (ucs = 2 mm and ucs = 5 mm) with a porosity of 70% show that the printed Schwarz-Diamond-TPSf structures exhibit no visible defects. The fabricated geometries closely match the designed surfaces, confirming excellent structural integrity at these configurations. This observation indicates that low unit cell sizes do not compromise structural conformity as long as the sheet thickness remains above the overmelting threshold. The analysis then focuses on samples with unit cell sizes of 10 mm and 20 mm, as these configurations reveal important trends in structural integrity. Due to their specific geometry, TPMS structures tend to show a self-supporting behaviour, that allows for their support-free manufacture at overhangs and curvatures that are outside of the common design limits presented in literature [13, 17–19]. However, as the unit cell size increases, this self-support effect decreases, leading to a higher risk of localized deformation, especially in regions with thin-walled features and high porosity. The results indicate that ucs = 10 mm leads to only minimal deviations, while ucs = 20 mm generally exhibits more pronounced local deviations. In particular, high porosity levels (ε = 90%) in combination with ucs = 20 mm result in significant deformations that compromise functionality.

At ε = 70% and ucs = 20 mm, the structure maintains its integrity but shows minor localized damage. These minor defects could potentially affect the functionality of the areas.

For ε = 80% and ucs = 20 mm, the results are similar to those observed for the 70% porosity structure. The overlay analysis shows a strong match between the designed and manufactured surfaces. However, minor localized damage is identified, indicating potential weaknesses in certain regions.

For ε = 90% and ucs = 10 mm, the printed structure closely matches the designed geometry. Only minor deviations are observed, and these do not affect overall functionality. This confirms that at moderate unit cell sizes, the structure remains stable even at high porosity levels. In addition, structures with ucs = 10 mm at 70% and 80% porosity, as well as those with ucs < 10 mm, did not exhibit these issues.

In contrast, the structure with ε = 90% and ucs = 20 mm shows significant damage. Thin-walled regions and complex geometries show significant deviations between the designed and printed surfaces, as highlighted by the overlay

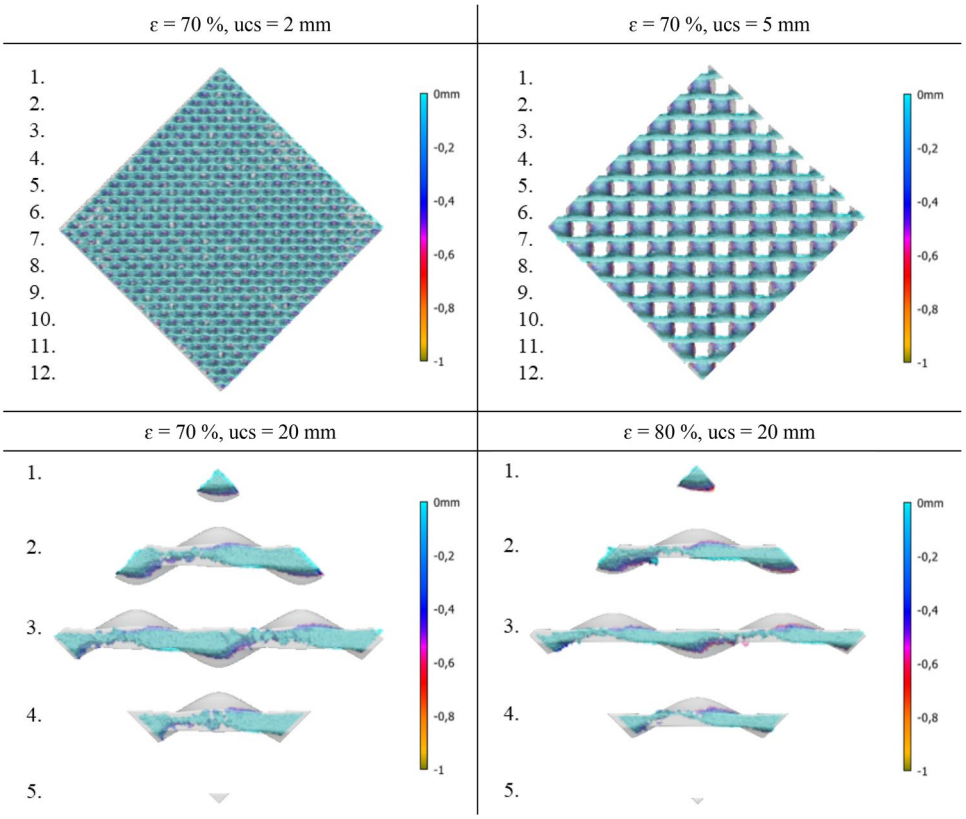

Fig. 5 Comparison of printed and designed Schwarz-Diamond-TPSf structures (ε = 70%, 80%, ucs = 2 mm, 5 mm, 20 mm)

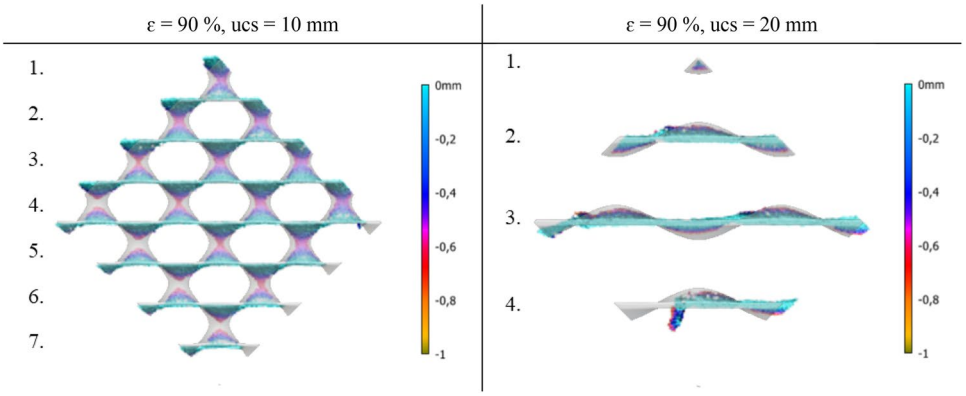

Fig. 6 Comparison of printed and designed Schwarz-Diamond-TPSf structures (ε = 90%, ucs = 10 mm, 20 mm)

analysis in Fig. 4. These defects compromise the structural integrity and make the component non-functional.

Building on the findings from the Schwarz-Diamond-TPSf structures, the evaluation is extended to Gyroid-TPSf structures to examine how their distinct geometry influences manufacturability and structural integrity (see Figs. 7 and 8).

Similar to the Schwarz-Diamond-TPSf structures, the Gyroid-TPSf structures with ucs = 2 mm and ucs = 5 mm at a porosity of 70% also show no detectable defects. At larger unit cell sizes, particularly at ucs = 20 mm, the Gyroid-TPSf structures show noticeable deviations and larger surface defects compared to the designed geometry in *nTopology*. These localized defects could potentially affect functionality in specific areas and can be attributed to the fact that, at a unit cell size of 20 mm, the structures are no longer self-supporting, leading to breakage or the presence of damaged regions. For ε = 90% and ucs = 10 mm, the structure successfully maintains its integrity with only minor deviations that do not affect its overall functionality.

4.4 Overview of printability

The diagrams in Figs. 9 and 11 illustrate the printability of the Gyroid-TPSf and Schwarz-Diamond-TPSf structures as a function of ε_t and ucs. Printability is defined as the ability of a structure to be successfully fabricated according to the design, and it strongly depends on key conditions

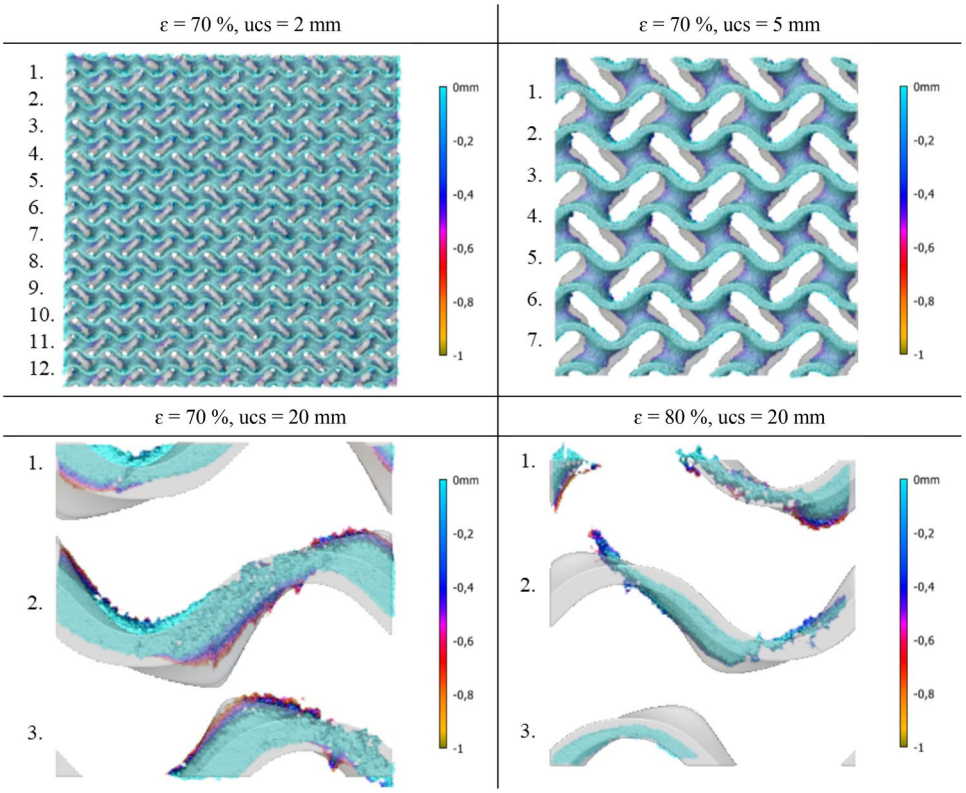

Fig. 7 Comparison of printed and designed Gyroid-TPSf structures (ε = 70%, 80%, ucs = 2 mm, 5 mm, 20 mm)

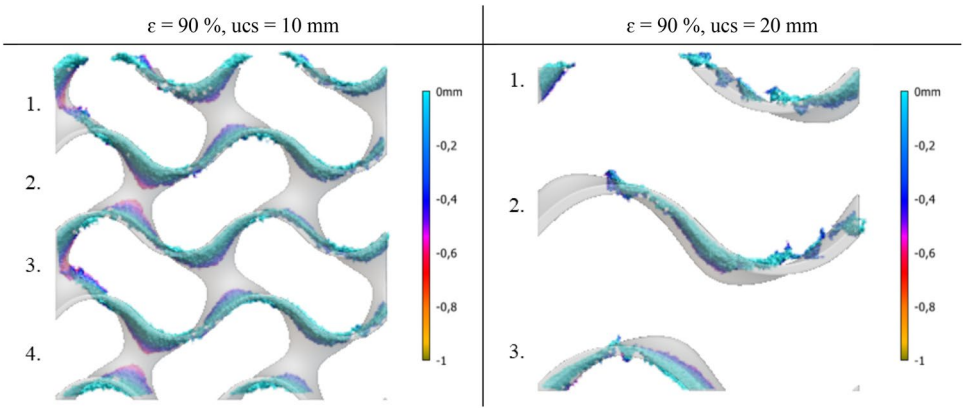

Fig. 8 Comparison of printed and designed Gyroid-TPSf structures (ε = 90%, ucs = 10 mm, 20 mm)

such as sheet thickness, porosity, and structural integrity. The classification in the diagrams follows three categories: 'Manufacturable as designed', 'Local deformation', and 'Incomplete/fragile', providing a clear indication of whether the structures meet the necessary requirements for successful manufacturing.

The diagram for the Gyroid-TPSf structures in Fig. 9 indicates that manufacturability is limited at unit cell sizes of ucs = 2 mm and ucs = 20 mm. This limitation arises due to two primary factors:

- At large unit cell sizes (e.g., ucs = 20 mm), the curvature radius of the structure decreases, reducing self-supporting effects. As a result, certain regions lack sufficient mechanical stability during the printing process, leading to deformation or failure (see Fig. 9, characterized by 'Local deformation').
- At small unit cell sizes and high porosity levels (e.g., ucs = 2 mm and ε_t = 90%), the resulting sheet thickness becomes critically thin, often below the printable resolution of the PBF-LB/M process. This leads to incomplete or fragile structures that fail during manufacturing, even if adapted parameters are used (see Fig. 9, characterized by 'Incomplete/fragile').

For ε_t = 70% and 80%, structures can be successfully printed at a medium unit cell size of ucs = 10 mm. Reducing the cell size to ucs = 5 mm still allows for successful

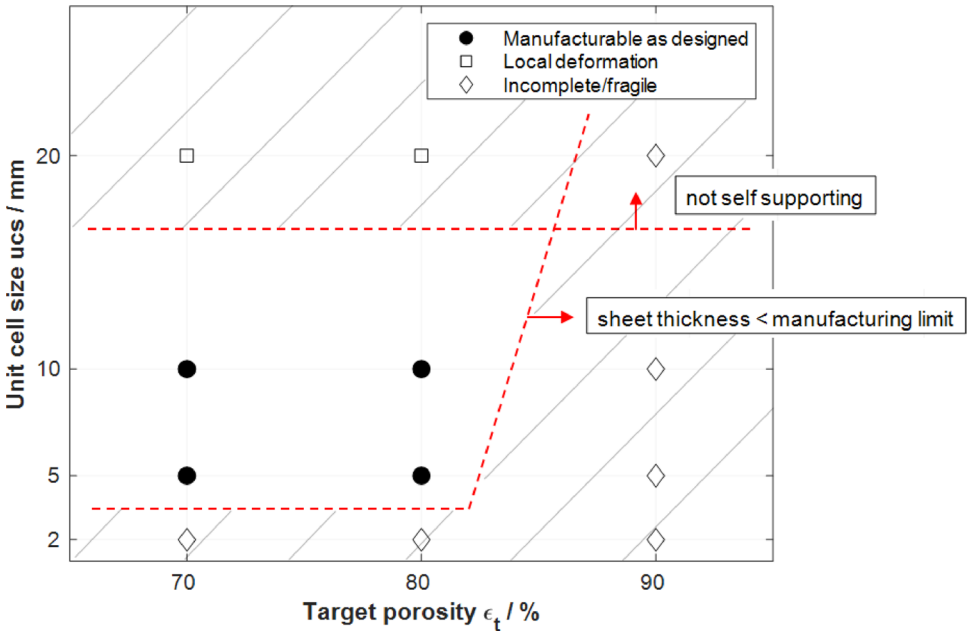

Fig. 9 Overview of printability for Gyroid-TPSf structures

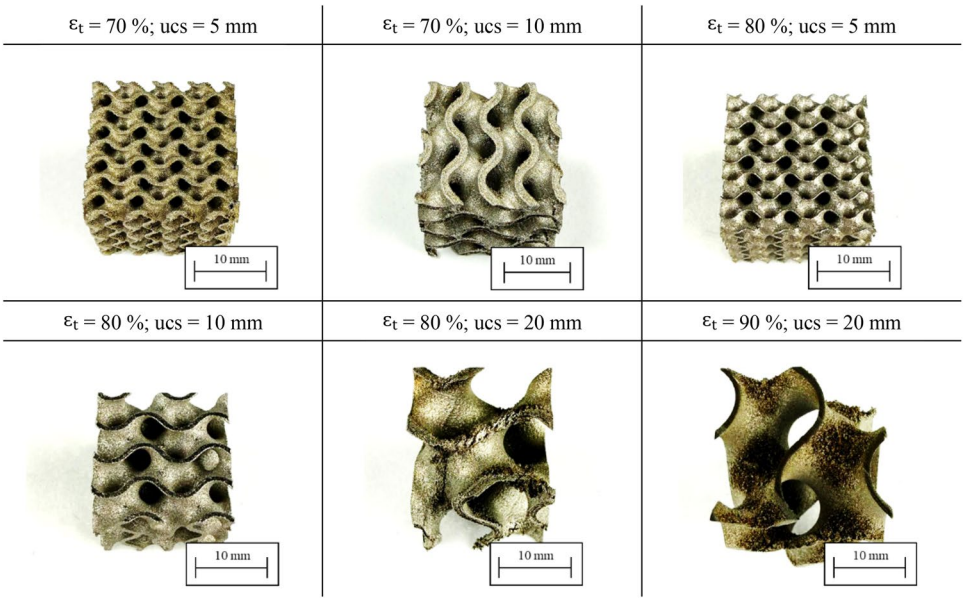

Fig. 10 Gyroid-TPSf structures with varying design parameters of target porosity (ε_t) and unit cell size (ucs). Successful prints at ε_t = 70% and ucs = 5 mm; ε_t = 70% and ucs = 10 mm, ε_t = 80% and ucs = 5 mm, ε_t = 80% and ucs = 10 mm. Failed prints at ε_t = 80% and ucs = 20 mm and ε_t = 90% and ucs = 20 mm

manufacturing at ε_t = 70% and 80%, but structures with ε_t = 90% fail at this scale.

Figure 10 shows several representative examples of printed Gyroid-TPSf structures with varying target porosities and unit cell sizes. The structures with ε_t = 70% and ucs = 5 mm or 10 mm, as well as ε_t = 80% and ucs = 5 mm or 10 mm, show successful prints characterized by sufficient sheet thickness and good structural stability. In contrast, the structures with ε_t = 80% and ucs = 20 mm and ε_t = 90% and ucs = 20 mm demonstrate failed prints due to insufficient sheet thickness and loss of structural integrity, highlighting the limitations associated with large unit cell sizes and high porosities.

For the Schwarz-Diamond-TPSf structure, the diagram in Fig. 11 shows a similar pattern as observed in the Gyroid-TPSf structure. The largest unit cell size (ucs = 20 mm) is unprintable for all target porosities due to local deformation. At ucs = 5 mm and 10 mm, structures remain manufacturable as designed for ε_t = 70% and 80%, maintaining sufficient stability. In contrast, structures with ucs = 2 mm across all target porosities are classified as incomplete or fragile, failing to meet the requirements for successful printability.

Figure 12 shows representative Schwarz-Diamond-TPSf structures with varying design parameters of ε_t and ucs. The structures with ε_t = 70% and ucs = 5 mm or 10 mm, as well as ε_t = 80% and ucs = 5 mm or 10 mm, show successful prints.

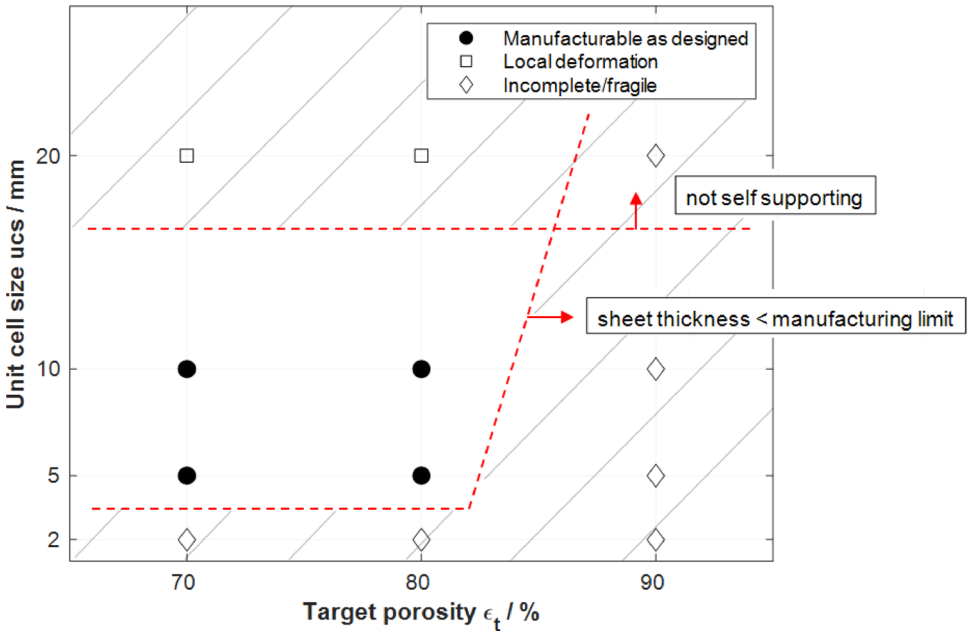

Fig. 11 Overview of printability for Schwarz-Diamond-TPSf structures

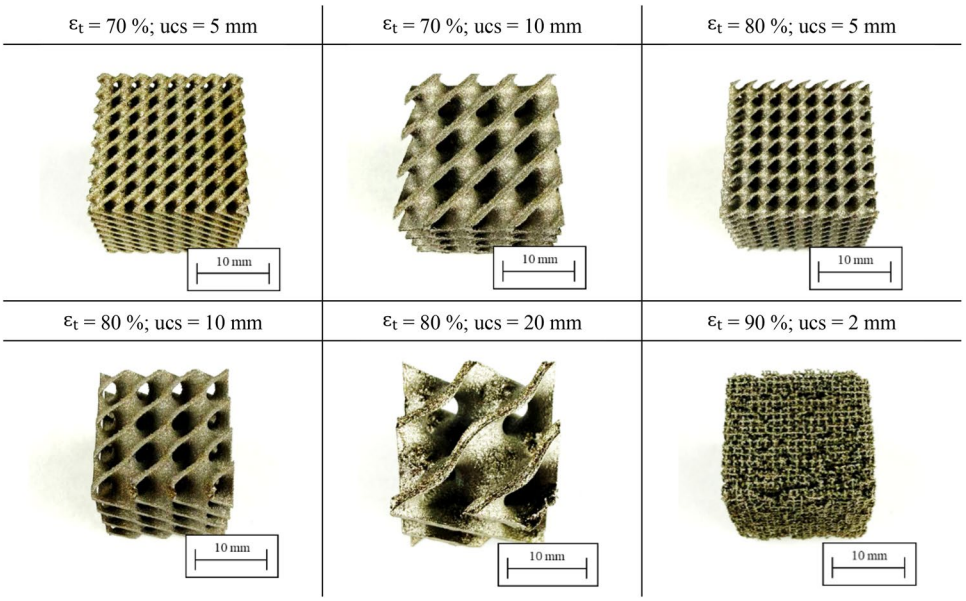

Fig. 12 Schwarz-Diamond-TPSf structures varying design parameters of target porosity (ε_t) and unit cell size (ucs). Successful prints at ε_t = 70% and ucs = 5 mm; ε_t = 70% and ucs = 10 mm, ε_t = 80% and ucs = 5 mm, ε_t = 80% and ucs = 10 mm. Failed prints at ε_t = 80% and ucs = 20 mm and ε_t = 90% and ucs = 20 mm

In contrast, the structures with ε_t = 80% and ucs = 20 mm and ε_t = 90% and ucs = 20 mm represent failed prints due to local deformation and fragile or incomplete features.

Furthermore, the comparison demonstrates that the difference in manufacturability between Gyroid- and Schwarz-Diamond-TPSf structures is marginal, with a slight advantage for Gyroid-TPSf due to slightly higher resulting sheet thickness values for identical porosity and unit cell sizes.

In addition to printability, surface roughness is a critical factor for smart reactor applications, impacting heat-transfer efficiency and overall performance. Although direct measurement on the complex, curved surfaces of the TPMS structures is challenging, wall samples fabricated under same printing parameters were analyzed to estimate surface roughness. Experimental measurements yielded an average S_a of 37.13 µm, highlighting the relatively rough as-printed surface. To improve surface quality, post-processing methods such as electrochemical polishing can be employed, which can reduce roughness and enhance performance where required.

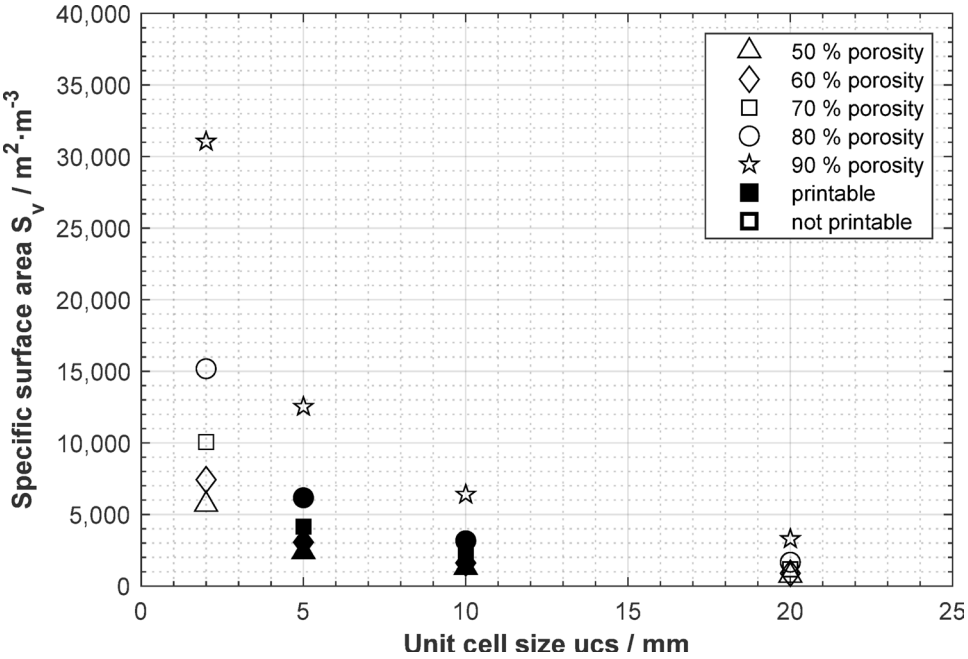

Fig. 13 Specific surface area as a function of the unit cell size for Gyroid-TPSf structures at different target porosity levels (50%, 60%, 70%, 80%, 90%)

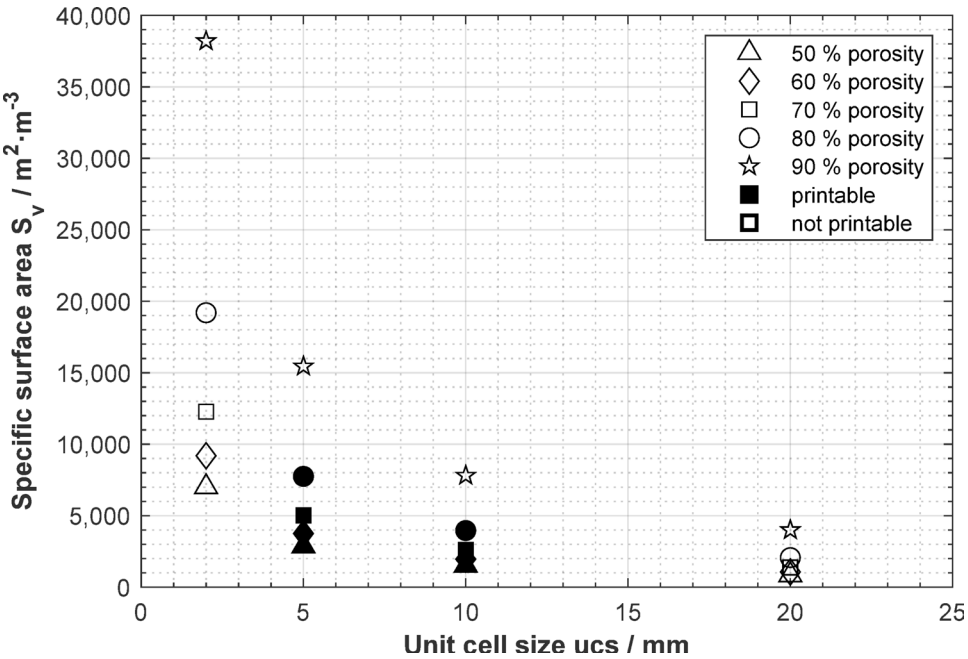

Fig. 14 Specific surface area as a function of the unit cell size for Schwarz-Diamond-TPSf structures at different target porosity levels (50%, 60%, 70%, 80%, 90%)

5 Relevance for applications in SMART Reactors

This section presents a comprehensive numerical analysis of Gyroid-TPSf and Schwarz-Diamond-TPSf structures, focusing on three key performance parameters for the application in SMART Reactors: specific surface area, pressure drop and heat transfer.

5.1 Surface area of Gyroid-TPSf and Schwarz-Diamond-TPSf

The specific surface area S_v is a critical parameter for many engineering applications, as it defines the available interaction surface per unit volume e.g. for catalytic reactions. The following section analyzes the results for S_v as a function of unit cell size and porosity. Figures 13 and 14 illustrate the relationship between the specific surface area and the unit cell size for Gyroid-TPSf and Schwarz-Diamond-TPSf, under varying target porosity values (50%, 60%, 70%, 80%,

and 90%). For both structures, the specific surface area decreases as the unit cell size increases. This trend is consistent across all target porosity levels, indicating that smaller unit cell sizes provide a higher surface-to-volume ratio. Moreover, higher porosities generally result in a higher specific surface area, as they create more open structures with thinner walls and increased surface exposure. Although the 50% and 60% porosity levels were not experimentally printed, it can be assumed that structures with unit cell sizes of 5 mm and 10 mm would also be printable due to their sufficient sheet thickness and structural stability. A comparison between the two structures shows that the Schwarz-Diamond-TPSf typically has a slightly higher specific surface area than the Gyroid-TPSf under identical conditions. This is due to the geometric properties of the Schwarz-Diamond surface, which inherently yields a larger surface area for a given volume. Therefore, Schwarz-Diamond-TPSf is particularly well-suited for applications requiring a high surface-to-volume ratio, such as heat exchangers or chemical reactors.

To contextualize the specific surface area of the Gyroid-TPSf and Schwarz-Diamond-TPSf structures, their geometric specific surface areas are compared to data from current industrial systems, such as monolithic reactors. In this comparison, the geometric surface area is used for both the monolithic structures and the TPSf structures, without accounting for internal porosity. Monolithic reactors typically exhibit a geometric specific surface areas ranging from approximately 650 to 4400 $m^2 \cdot m^{-3}$ [28, 29], placing the printable TPMS structures within the same order of magnitude or even exceeding these values. Notably, TPMS structures offer a significant advantage over monolithic configurations: their geometric morphology can be tailored with high flexibility to meet specific application requirements.

5.2 Pressure drop of Gyroid-TPSf and Schwarz-Diamond-TPSf

In engineering systems with integrated porous structures, pressure drop serves as a key metric for assessing flow patterns and overall energy efficiency. In TPMS porous structures in particular, the morphology significantly influences the flow characteristics, which in turn directly dictate the pressure drop. Contributing factors for porous structures comprise continuous changes in flow direction, flow acceleration and deceleration in strut channels, mixing in nodes, and the contact area between the fluid and solid surface. Furthermore, the degree of wall coupling is also relevant. To comprehend the impact of the morphology on the flow characteristics, the focus of the geometrical analysis of TPMS porous structures is on the number of nodes, struts per node and the constitution of pores inside a unit cell. For the Schwarz-Diamond-TPSf structure consistently increased pressure drop is observed owing to its complex network of multiple node composition and the dramatic changes in flow direction [30]. This section presents both experimental investigations and computational fluid dynamics (CFD) simulations. The experiments serve as a reference case for validating the CFD model. Subsequently, the CFD simulations are employed to analyze all structures that are considered printable via PBF-LB/M with sufficient quality. Apart from the morphology of the structure, the porosity depending on the sheet thickness and unit cell size are investigated towards their contribution to the drag coefficient, i.e., pressure drop. The following section describes the experimental setup, followed by a detailed presentation of the computational domain used for the CFD simulations.

For the experiments, an exemplary printed Schwarz-Diamond-TPSf part with a unit cell size of 5 mm and a porosity of 70% is analyzed. The experimental setup, illustrated in Fig. 15a and b, comprises a pump *(Gather Industries GmbH, Germany)*, a Coriolis mass flow meter *(Promass*

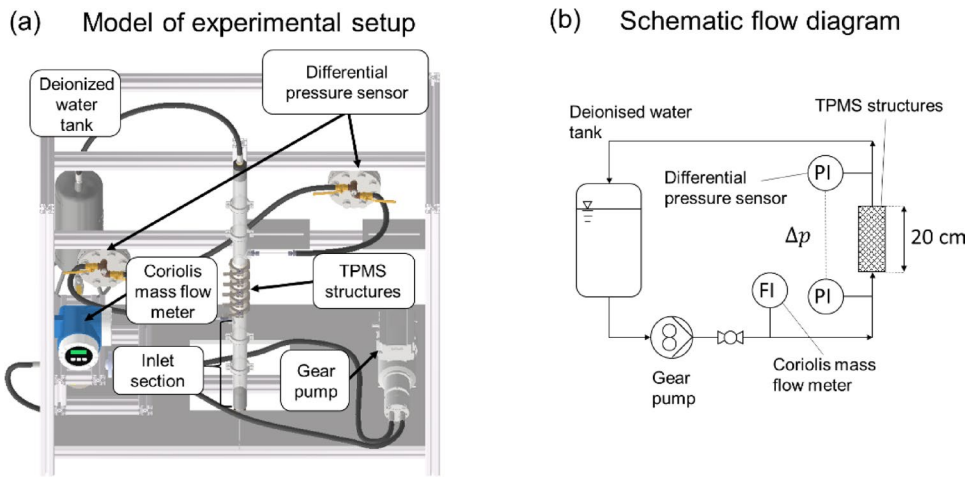

Fig. 15 Experimental setup for pressure drop measurements with a model of the experimental setup detailing the acrylic pipe, the TPMS, and associated peripheral systems in **a** and a schematic flow diagram of the experimental setup in **b**

80, Endress+Hauser, Switzerland) for measuring the mass flow rate, and a differential pressure sensor *(Smar Technology Company, Brazil)*. The pump conveys deionized water into a vertical acrylic glass DN 40 pipe with a diameter of d=38 mm before directing it into the additive manufactured packing. The inlet length before the flow enters the structure is L=400 mm, which helps to stabilize the flow and minimize entrance effects. To avoid the formation of channels between the structure and the pipe wall—commonly observed when the structure is merely inserted into the pipe and which can influence the pressure drop—the pipe wall is directly printed onto the structure in this study [31]. Figure 16 presents an example of such an element. The inner diameter of the structure corresponds to the pipe diameter, with an element height h=40 mm. To generate higher pressure drops within the measurable range of the differential pressure sensor, five elements are connected in series.

The deionized water is maintained at a constant temperature $T = (19.9 \pm 0.5)\ °C$, with a corresponding fluid density $\rho = (998.0 \pm 0.1)\ \mathrm{kg\ m^{-3}}$ and a viscosity $\eta = 1 \cdot 10^{-3}$ [32]. The experiments are conducted in the laminar flow regime within the open pipe, characterized by a Reynolds number $\mathrm{Re} < 2300$ [33]. The Reynolds number is defined as

$$\mathrm{Re} = \frac{\rho d v}{\eta} \tag{3}$$

Fig. 16 An additively manufactured module featuring a TPMS structure, directly connected to the wall, used for the pressure drop study

where v represents the mean velocity in the pipe. For TPMS porous structures, the respective Reynolds number $\mathrm{Re_h}$ is defined via

$$\mathrm{Re_h} = \frac{v \cdot D_h}{\nu \cdot \in} \tag{4}$$

with the hydraulic diameter D_h based on particular geometric features, which can be calculated from the total wetted surface area A and porosity $\in$

$$D_h = \frac{4 \cdot \in \cdot V}{A} \tag{5}$$

The pressure sensors are calibrated using hydrostatic pressure. The hydrostatic pressure $p(h)$ on the lower pressure sensor is directly proportional to the height of the liquid level h as described in Eq. (6). For a fluid with constant density, the hydrostatic pressure is given by Pascal's law as

$$p(h) - p_0 = \rho g h \tag{6}$$

where $p_0 = 1$ atm denotes the atmospheric pressure and $g = 9.81\ \mathrm{m\ s^{-2}}$ the gravitational acceleration [33]. A transparent tube is integrated into the setup, enabling the water column height to be determined optically in 1 cm (with an uncertainty of ± 0.1 cm) increments. The resulting pressure data are then correlated with the sensor measurement signals via a quadratic fitting function. In addition to the hydrostatic pressure, the pressure drop Δp according to Eq. (7) is added in a flow-through system.

$$\Delta p_{\mathrm{total}} = \rho g h + \Delta p \tag{7}$$

The total pressure change consists of the hydrostatic pressure and an additional pressure drop. In the context of differential pressure measurement, two components contribute to the pressure drop: the pipe itself and the TPMS structures. The pressure sensors are positioned 5 cm upstream and downstream of the packing. The additional pressure drop Δp_{pipe} induced by the pipe itself can be estimated using Hagen-Poiseuille's law

$$\Delta p_{\mathrm{pipe}} = \frac{128 \dot{V} \eta L_{\mathrm{pipe}}}{\pi d^4} \tag{8}$$

for a laminar flow. $\dot{V}$ denotes the volumetric flow rate and L_{pipe} is the length of the section. For all examined flow velocities, this additional pressure drop remains below 0.015 Pa and is therefore considered negligible [33]. In addition to the experimental investigations, CFD simulations

were also conducted, the methodology and results of which are detailed in the following sections.

The simulations are performed using the open-source software *OpenFOAM (version 2212)*. Due to their periodic nature, the simulations are conducted for a representative elementary volume (Fig. 17), as this approach yields results comparable to full-scale simulations involving multiple unit cells per cross section [34]. To cover potential entrance and exit effects and to maintain similarities to the experimental setup, an excessive entrance and exit length of 1–2 ·ucs is selected. Inlet velocity and pressure outlet boundary conditions are applied in combination with periodic boundary conditions along the four sides of the domain to account for the repetitive pattern of TPMS structures. For this setup, a grid convergence study is performed for the Schwarz-Diamond-TPSf structure with a porosity ϵ_t of 70% and a unit cell size of 5 mm to ensure the accuracy of the simulations results for comparison with experimental validation. Convergence is confirmed for a representative cell size Δx of 66.96 µm, defined as the cubic root of the average cell volume (Eq. 9), indicating that further mesh refinement has a negligible effect on the solution. Meshes generated with *snappyHexMesh* are predominantly unstructured, consisting mainly of hexahedral cells with local refinements and transitions to polyhedral cells near complex geometries.

$$\Delta x = \left[\frac{1}{\mathrm{N}} \sum_{\mathrm{i}=1}^{\mathrm{N}} \Delta V_{\mathrm{i}} \right]^{\frac{1}{3}} \tag{9}$$

Unsteady laminar flow regime is defined for flows through porous media between $200 < \mathrm{Re_h} < 350$ [35]. Therefore, *simpleFoam* is employed as a solver, as it is capable of handling steady, incompressible flow of Newtonian fluids. All structures are evaluated at $\mathrm{Re} = 1140$.

The k-ω SST turbulence model is chosen for its accurate near-wall predictions and its ability to handle complex geometries with separated and recirculating flows, as backflow inside the Schwarz-Diamond-TPSf porous structure was already reported even for low $\mathrm{Re_h}$ [30]. Gradient and diffusion terms are discretized using primarily second-order accurate schemes with limiting for stability in regions of high gradients, while divergence terms use a mix of second-order upwind for the velocity field and limited linear schemes for turbulence parameters. Time discretization is first-order accurate using the implicit Euler method.

Figure 18 presents a comparison between the experimental data and the simulation results. The measured pressure drop deviates from the simulated data, with the simulation overestimating the pressure drop by approximately 21%. The following hypothesis is proposed to explain this deviation. Our hypothesis for the observed reduction in pressure drop is the presence of entrapped gas bubbles on the surface of the structure. The formation of these bubbles can be attributed to two primary factors. First, the deionized water used is saturated with dissolved gases. Due to the pressure drop within the structure, the solubility of these dissolved gases decreases, leading to bubble formation via outgassing. Second, the surface roughness of the structure facilitates the entrapment of bubbles, thereby reducing the overall pressure drop. The average surface roughness, measured using a profilometer (*Keyence Corporation, Japan*), is 62.7 µm. This level of roughness enhances gas bubble adhesion, creating a slip effect that is known to decrease pressure drop. This surface roughness promotes the adhesion of gas bubbles, resulting in a slip effect that is known to significantly reduce pressure drop [36]. This phenomenon is qualitatively supported by observations made during ethanol flushing: due to its higher solubility for air, microbubbles became visibly detached from the surface. Furthermore, during the actual water-based measurements, coalesced bubbles were observed emerging from the TPMS structure. Moreover, the structure exhibits a twisted geometry, which facilitates the entrapment of gas bubbles. These bubbles can block portions of the structure and induce local channeling, thereby further altering the pressure drop.

As there was no continuous gas layer covering the entire TPMS surface, the slip effect was only partial. Some regions contained trapped bubbles, while others remained free of bubbles, resulting in a heterogeneous slip condition. Consequently, the CFD simulations were iteratively adjusted to reflect a partial slip condition of 30% across the full measurement range. The results of the pressure drop measurements with the results of the adapted CFD simulations

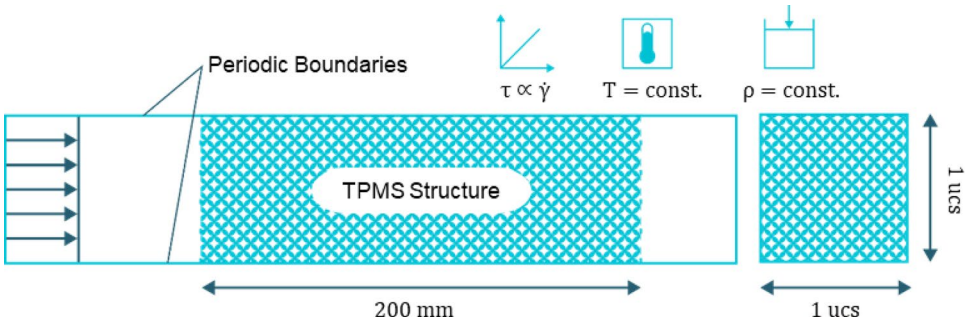

Fig. 17 Computational domain for numerical flow simulations with periodic boundary configuration

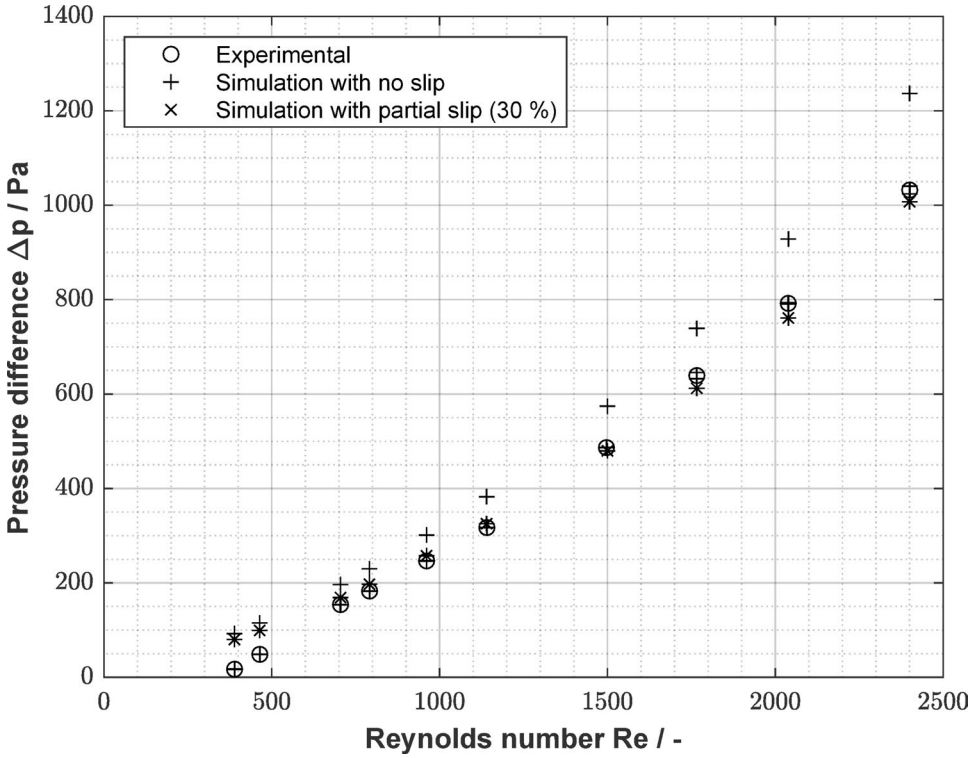

Fig. 18 Comparison with experimental pressure drop and CFD simulation for the Schwarz-Diamond TPSf with a ucs = 5 mm and a porosity of 70%

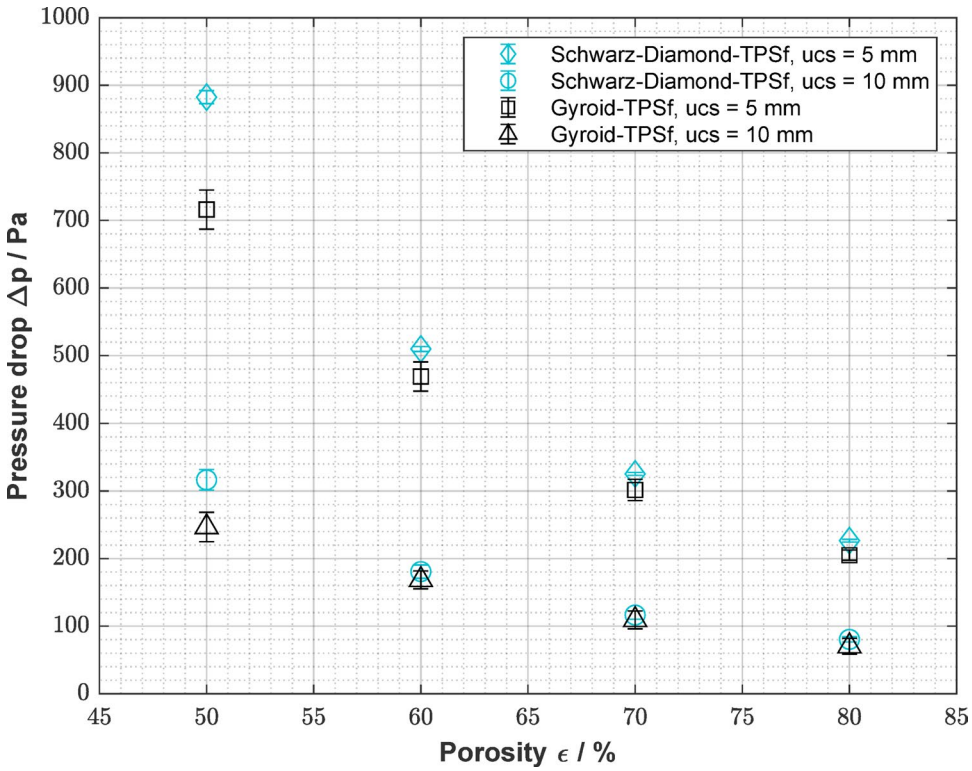

Fig. 19 Comparison of Gyroid-TPSf and Schwarz-Diamond-TPSf with different unit cell sizes of 5 mm and 10 mm showing pressure drop vs. porosity

are shown in Fig. 18. With this adjustment, the simulation results aligned well with the experimental data, and the partial slip condition is therefore applied in all subsequent simulations.

Figure 19 presents the relation of the pressure drop Δp to the unit cell size ucs and porosity ε_t for the Schwarz-Diamond-TPSf and Gyroid-TPSf. Both TPMS structure exhibit the same trend. As the permeability increases for porosity and also unit cell size, a corresponding decrease

in the pressure is observed in the CFD simulations. Differences between Gyroid-TPSf and Schwarz-Diamond-TPSf are more pronounced for lower porosities, whereas at higher porosities they become negligible, despite only minor changes in overall surface area. This indicates that flow acceleration and deceleration in strut channels are key contributors to the observed pressure drop behavior. For smaller unit cell sizes, the wetted surface area is noticeably lower. Thus, interactions between the fluid and solid surface contribute less to the overall pressure drop.

5.3 Heat transfer in Gyroid-TPSf and Schwarz-Diamond-TPSf

To further assess the potential of TPMS structures in process engineering and especially in SMART reactors, the heat transfer performance of such structures is additionally studied using CFD. This investigation is interesting due to the intrinsic geometric complexity and the strong interdependence between morphology, transport phenomena, and boundary conditions. The intricate topology of TPMS structures introduces local variations in curvature, surface orientation, and channel connectivity that can directly influence convective and conductive heat transfer. Differences in porosity, topology, and local curvature may influence boundary-layer development and convective mixing, thereby affecting the overall heat transfer performance. In this study, special emphasis is placed on examining how the unit cell size influences these heat transfer characteristics.

Heat transport is modeled using a passive scalar that represents a normalized temperature field $\mathrm{T} \in [0,1]$. The temperature distribution is computed on a steady-state velocity field obtained from the preceding numerical flow simulations. The corresponding boundary conditions are summarized in Table 3. It is assumed that the thermal conductivity of the TPMS structure is significantly higher than the heat flux transferred to the fluid phase. Thus, a Dirichlet boundary condition is imposed on the TPMS surface, maintaining a constant temperature at the solid–fluid interface.

For the two investigated structures, namely the Schwarz-Diamond-TPSf and the Gyroid-TPSf, heat transfer is evaluated using the Nusselt number

$$\mathrm{Nu} = \frac{\alpha \cdot \mathrm{L}}{\lambda}, \tag{10}$$

Table 3 Boundary Conditions for heat transfer simulations

Computational zone	Boundary (Type)	Expressions
Fluid	Inlet (Velocity Inlet)	$\mathrm{T} = \mathrm{T_{in}}$
	TPMS structure (Wall)	$\mathrm{T} = \mathrm{T_{Wall}}$
	Periodic boundary (CyclicAMI)	$\mathrm{T_{Patch\ A}} = \mathrm{T_{Patch\ B}}$
	Outlet (Pressure outlet)	$\nabla \mathrm{T} \cdot \mathrm{n} = 0$

which is determined for each individual unit cell. The heat flux $\dot{\mathrm{Q}}$ is obtained from the mean fluid temperatures at the inlet $\overline{\mathrm{T}}_{\mathrm{i}}$ and outlet $\overline{\mathrm{T}}_{\mathrm{i+1}}$ of a single unit cell

$$\dot{\mathrm{Q}} = \dot{\mathrm{m}} \cdot \mathrm{c_p} \cdot \left(\overline{\mathrm{T}}_{\mathrm{i+1}} - \overline{\mathrm{T}}_{\mathrm{i}}\right) = \mathrm{A} \cdot \alpha \cdot \left(\mathrm{T_{wall}} - \frac{\overline{\mathrm{T}}_{\mathrm{i+1}} + \overline{\mathrm{T}}_{\mathrm{i}}}{2}\right) \tag{11}$$

as from which the heat transfer coefficient α is derived (Eq. 10). For this reason, the mesh resolution is adjusted, so that the temperature gradients in near wall regions are resolved. Hence, the heat transfer coefficient is simulated in the process. As the heat transfer approaches completion near the outlet of the structures, the Nusselt number is evaluated on a unit-cell basis to enhance sensitivity.

As the heat transfer coefficient is primarily governed by the morphology of the structure, which remains almost constant along the reactor, the overall heat transfer performance is also uniform (Fig. 20). For the calculation of the average Nusselt number, only regions exhibiting a significant heat flux (positions where $\overline{\mathrm{T}} < 0.95$) are considered to ensure reliability. Cheng et al. [29] investigated the influence of geometrical features and porosity on the heat transfer characteristics of TPMS structures. In the present work, the unit cell size is introduced as an additional parameter. Considering the constraints imposed by additive manufacturing (Figs. 9 and 11) unit cell sizes of 5 mm and 10 mm were analyzed using CFD. Figure 21 shows the variation of the Nusselt number with porosity for both structures. The Schwarz-Diamond-TPSf and the Gyroid-TPSf exhibit trends consistent with previous findings, with the Schwarz-Diamond-TPSf demonstrating superior heat transfer performance for a unit cell size of 5 mm. For comparison, the results for representative cases are summarized in Table 4. Moreover, a reduction in unit cell size leads to a decrease of the Nusselt number. Since higher porosity structures exhibit superior heat transfer characteristics, further research into advanced printing techniques that enable reduced sheet thickness while maintaining structural integrity is strongly advised.

6 Conclusion and Outlook

This study investigated the design and manufacturability of TPMS structures, specifically the Gyroid-TPSf and Schwarz-Diamond-TPSf geometries, through PBF-LB/M using 316L stainless steel. By analyzing the interplay between unit cell size, porosity and sheet thickness, practical design guidelines were established to optimize the fabrication process for TPMS-based structures.

The results highlight that manufacturability is strongly influenced by unit cell size and porosity, with medium unit

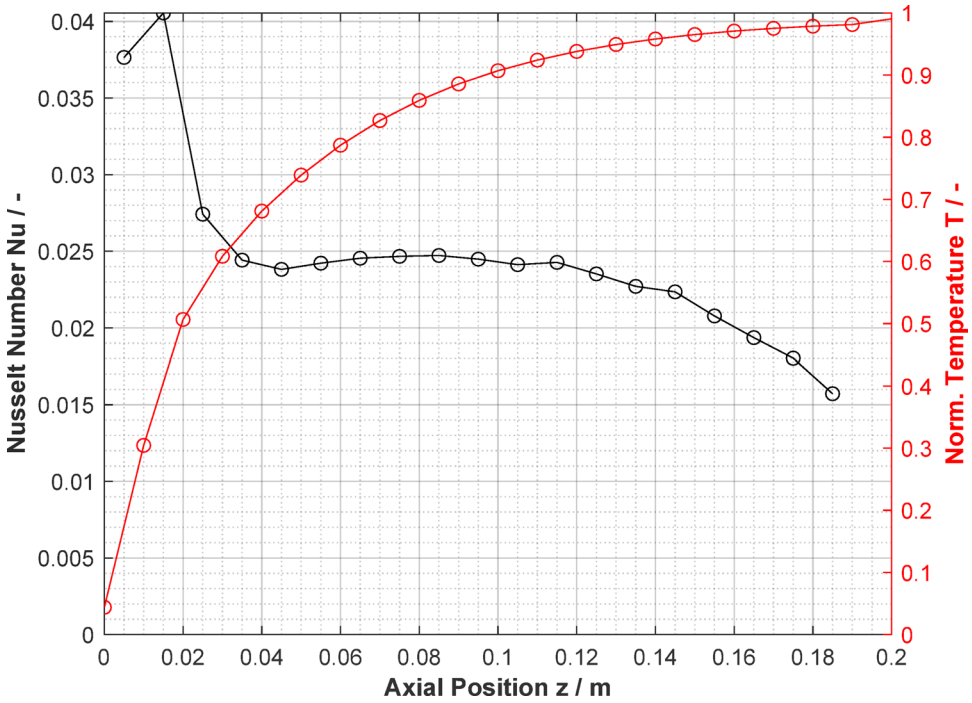

Fig. 20 Nusselt number over the length of the Schwarz-Diamond-TPSf structure (ucs = 10 mm, ε = 70%)

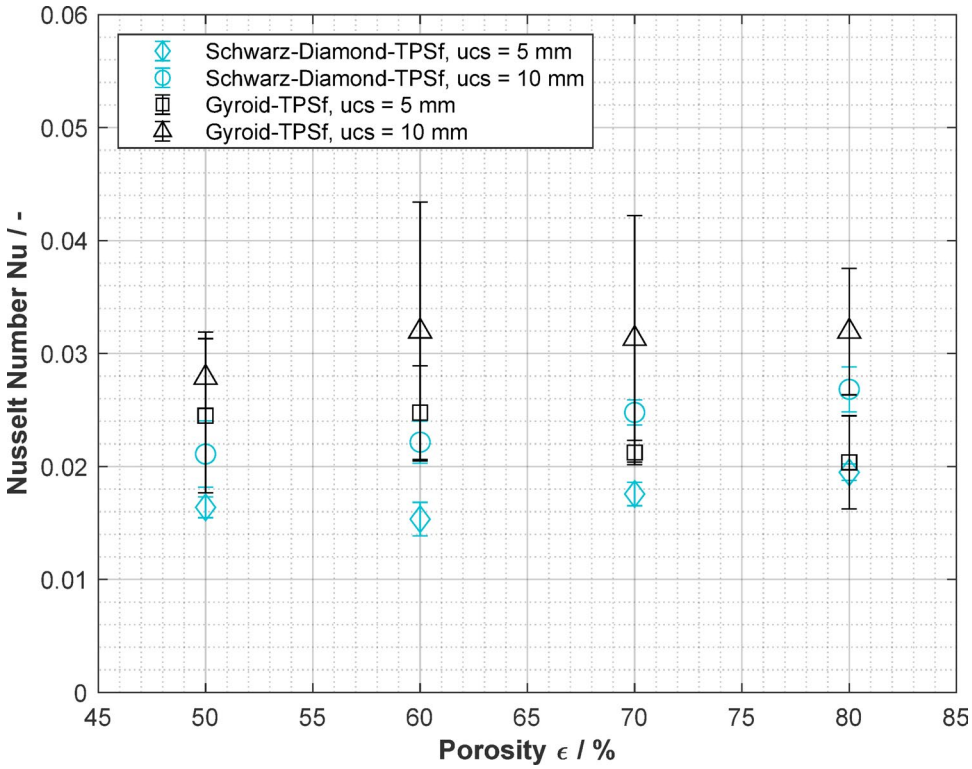

Fig. 21 Average Nusselt number for all printable TPMS structures

Table 4 Overview of key performance indicators for TPMS in process engineering applications

Type	ε/%	ucs/mm	Δp/Pa	Nu/-
Schwarz-Diamond-TPSf	80	5	227 ± 2	0.0195 ± 0.0007
Schwarz-Diamond-TPSf	80	10	80 ± 4	0.0274 ± 0.0037
Gyroid-TPSf	80	5	205 ± 8	0.0204 ± 0.0041
Gyroid-TPSf	80	10	70 ± 12	0.0311 ± 0.0059

cell sizes (ucs = 5 mm and 10 mm) and moderate porosities (ε_t = 70% and 80%) yielding successful prints. In contrast, small unit cell sizes (ucs = 2 mm) and large unit cell sizes (ucs = 20 mm) led to structural defects or complete print failures, primarily due to the limitations of the process resolution and melt pool size in the PBF-LB/M system.

A detailed analysis of the deviation of porosity showed that discrepancies between target and measured porosity increased with higher target porosity levels and smaller unit cell sizes. Specifically, structures with ucs = 2 mm and ε_t = 70% and 80% exhibited the largest deviation from the nominal porosity, indicating that porosity accuracy decreasing with increasing structural complexity and smaller structural dimensions.

Subsequent evaluation of the resulting sheet thickness confirmed that these porosity deviations are a direct result of the realized sheet thicknesses. Structures with a unit cell size of 2 mm and target porosities of 70% and 80% did not meet the IT10 tolerance class, primarily due to the limitations of the focal diameter of 55 µm of the commercial PBF-LB/M system used, which challenges the reproduction of features below 0.25 mm. In contrast, increasing the unit cell size to 5–20 mm reduced the deviation from the target sheet thickness.

When comparing both TPMS types, the Gyroid- and Schwarz-Diamond-TPSf structures exhibit nearly identical trends for the same ucs–porosity combinations, slightly favoring Gyroid-TPSf structures due to their minimally higher target sheet thickness values.

The structural integrity assessment confirmed that structures with ucs = 10 mm at 70% and 80% porosity and those with ucs < 10 mm maintained their designed geometry, whereas higher unit cell sizes (ucs = 20 mm) led to significant structural defects, making them unsuitable for practical applications.

The numerical evaluation of specific surface area demonstrated that Schwarz-Diamond-TPSf structures generally exhibited a higher specific surface area than Gyroid-TPSf structures, making them more effective in applications requiring a high surface-to-volume ratio, such as heat exchangers and chemical reactors.

Furthermore, both structures were investigated experimentally and numerically with respect to pressure drop. The CFD simulations for the Schwarz-Diamond-TPSf structure (ε = 70%, ucs = 5 mm) were validated against experimental data across various volume flow rates. Similar trends were observed for both structures: (a) lower porosity leads to more pronounced flow acceleration and deceleration, and (b) smaller unit cell sizes exhibit an increase in surface area, thereby enhancing the fluid–solid interaction. Furthermore, the study on heat transfer shows that variations in unit cell size can influence heat transfer characteristics. This work thus enables a knowledge-based selection of a suitable type of TPMS and its design parameters depending on the required flow characteristics in a given process engineering task while maintaining manufacturability.

To improve the applicability of TPMS structures in industrial environments, future research should focus on refining process parameters to improve geometric accuracy. In addition, exploration of alternative materials beyond 316L stainless steel could expand the use of TPMS structures in high performance environments that require increased strength, corrosion resistance or thermal stability. Another consideration is the incorporation of walls into TPMS structures. This modification could help reduce local deformation at the edges, thereby improving overall structural integrity and performance.

TPMS structures hold great promise for improving heat and mass transfer in demanding applications such as SMART reactors. However, the results highlight the need for further refinement of design and manufacturing processes to fully exploit their benefits.

Acknowledgements None.

Author contribution Conceptualization: Serhan Acikgöz, Christoph Wigger, Timo Merbach, Maria Isabelle Maiwald, Dr.-Ing. Dirk Herzog, Dr.-Ing. Felix Kexel, Prof. Dr.-Ing. Ingomar Kelbassa, Prof.-Dr-Ing. Michael Schlüter; Methodology: Serhan Acikgöz, Christoph Wigger, Timo Merbach, Maria Isabelle Maiwald, Dr.-Ing. Dirk Herzog, Prof. Dr.-Ing. Ingomar Kelbassa, Prof.-Dr-Ing. Michael Schlüter; Formal analysis and investigation: Serhan Acikgöz, Christoph Wigger, Timo Merbach, Maria Isabelle Maiwald, Dr.-Ing. Dirk Herzog, Prof. Dr.-Ing. Ingomar Kelbassa, Prof.-Dr-Ing. Michael Schlüter; Writing—original draft preparation: Serhan Acikgöz, Christoph Wigger, Timo Merbach; Writing—review and editing: Dr.-Ing. Dirk Herzog, Dr.-Ing. Felix Kexel, Prof. Dr.-Ing. Ingomar Kelbassa, Prof.-Dr-Ing. Michael Schlüter; Funding acquisition: Prof.-Dr-Ing. Michael Schlüter; Resources: Dr.-Ing. Dirk Herzog, Prof. Dr.-Ing. Ingomar Kelbassa, Prof.-Dr-Ing. Michael Schlüter; Supervision: Dr.-Ing. Dirk Herzog, Prof. Dr.-Ing. Ingomar Kelbassa, Prof.-Dr-Ing. Michael Schlüter.

Funding Open Access funding enabled and organized by Projekt DEAL. This research is funded by the Deutsche Forschungsgemeinschaft (DFG, German Research Foundation) – SFB 1615-503850735 – TP C01 & B04.

Data availability The dataset is available at: https://doi.org/10.15480/882.15954

Declarations

Competing interests The authors declare no competing interests.

Ethics approval and consent to participate Not applicable.

Consent for publication Not applicable.

References

1. DIN Deutsches Institut für Normung e.V. Additive fertigung – grundlagen – terminologie (ISO/ASTM 52900:2021); Deutsche fassung EN ISO/ASTM 52900:2021. 52900:2022-03, Berlin
2. Bhargava SK, Ramakrishna S, Brandt M, Selvakannan P (2022) Additive manufacturing for chemical sciences and engineering. Springer, Singapore, p 342
3. Al-Ketan O, Rowshan R, Abu Al-Rub RK (2018) Topology-mechanical property relationship of 3D printed strut, skeletal, and sheet based periodic metallic cellular materials. Addit Manuf 19:167–183. https://doi.org/10.1016/j.addma.2017.12.006
4. Fisher JW, Miller SW, Bartolai J, Simpson TW, Yukish MA (2023) Catalog of triply periodic minimal surfaces, equation-based lattice structures, and their homogenized property data. Data Brief 49:109311. https://doi.org/10.1016/j.dib.2023.109311
5. Feng J, Fu J, Yao X, He Y (2022) Triply periodic minimal surface (TPMS) porous structures: from multi-scale design, precise additive manufacturing to multidisciplinary applications. Int J Extrem Manuf 4(2):22001. https://doi.org/10.1088/2631-7990/ac5be6
6. Yeranee K, Rao Y (2022) A review of recent investigations on flow and heat transfer enhancement in cooling channels embedded with triply periodic minimal surfaces (TPMS). Energies 15(23):8994. https://doi.org/10.3390/en15238994
7. Holyst R (2005) Infinite networks of surfaces: an effective route to investigate complex periodic motifs in liquid crystals reveals that molecular packing alone can result in a tricontinuous network of channels separated by two periodic surfaces
8. Qu S, Ding J, Song X (2021) Achieving triply periodic minimal surface thin-walled structures by micro laser powder bed fusion process. Micromachines. https://doi.org/10.3390/mi12060705
9. Tang W, Zhou H, Zeng Y, Yan M, Jiang C et al (2023) Analysis on the convective heat transfer process and performance evaluation of triply periodic minimal surface (TPMS) based on Diamond, Gyroid and Iwp. Int J Heat Mass Transf 201:123642. https://doi.org/10.1016/j.ijheatmasstransfer.2022.123642
10. Granados MXC (2023) Study of triply periodic minimal surfaces for heat transfer applicationss
11. Kladovasilakis N, Tsongas K, Kostavelis I, Tzovaras D, Tzetzis D (2022) Effective mechanical properties of additive manufactured triply periodic minimal surfaces: experimental and finite element study. Int J Adv Manuf Technol 121(11–12):7169–7189. https://doi.org/10.1007/s00170-022-09651-w
12. Naghavi SA, Tamaddon M, Marghoub A, Wang K, Babamiri BB et al (2022) Mechanical characterisation and numerical modelling of TPMS-based gyroid and diamond Ti6Al4V scaffolds for bone implants: an integrated approach for translational consideration. Bioengineering (Basel, Switzerland). https://doi.org/10.3390/bioengineering9100504
13. Jones AD (2022) Design and additive manufacturing of TPMS-like cellular structures
14. Dr. Habil PD, Monika J (2025) Technische universität hamburg SFB 1615 SMART reactors. https://www.tuhh.de/sfb1615/welcome. Accessed 25 Sept 2025
15. Sun S, Brandt M, and Easton M (2017) Powder bed fusion processes. Laser Addit Manuf 55–77
16. Otto M, Pilz S, Gebert A, Kühn U, Hufenbach J (2021) Effect of build orientation on the microstructure, mechanical and corrosion properties of a biodegradable high manganese steel processed by laser powder bed fusion. Metals 11(6):944. https://doi.org/10.3390/met11060944
17. Adam GAO, Zimmer D (2015) On design for additive manufacturing: evaluating geometrical limitations. Rapid Prototyp J 21(6):662–670. https://doi.org/10.1108/RPJ-06-2013-0060
18. Kranz J, Herzog D, Emmelmann C (2015) Design guidelines for laser additive manufacturing of lightweight structures in $TiAl_6V_4$. J Laser Appl. https://doi.org/10.2351/1.4885235
19. Herzog D, Asami K, Scholl C, Ohle C, Emmelmann C et al (2022) Design guidelines for laser powder bed fusion in Inconel 718. J Laser Appl. https://doi.org/10.2351/7.0000508
20. Karcher H and Polthier K (1997) Construction of triply periodic minimal surfaces
21. Wakjira Y, Cioni A, Lemu HG (2024) Current status of the application of additive-manufactured TPMS structure in bone tissue engineering. Prog Addit Manuf. https://doi.org/10.1007/s40964-024-00714-w
22. Attarzadeh R, Attarzadeh-Niaki S-H, Duwig C (2022) Multi-objective optimization of TPMS-based heat exchangers for low-temperature waste heat recovery. Appl Therm Eng 212:118448. https://doi.org/10.1016/j.applthermaleng.2022.118448
23. Reynolds BW, Fee CJ, Morison KR, Holland DJ (2023) Characterisation of heat transfer within 3D printed TPMS heat exchangers. Int J Heat Mass Transf 212:124264. https://doi.org/10.1016/j.ijheatmasstransfer.2023.124264
24. Lu C, Zhang Y, Aziz M, Wen P, Zhang C et al (2022) Mechanical behaviors of multidimensional gradient gyroid structures under static and dynamic loading: a numerical and experimental study. Addit Manuf 59:103187. https://doi.org/10.1016/j.addma.2022.103187
25. Haas B (2023) 316L: ASTM A276/DIN EN 10088/1.4404 material data sheet
26. Yan C, Hao L, Yang L, Hussein AY, Young PG et al (2021) Design of TPMS structures triply periodic minimal surface lattices additively manufactured by selective laser melting. Elsevier, Amsterdam, pp 27–38
27. Wu Z, Narra SP, Rollett A (2020) Exploring the fabrication limits of thin-wall structures in a laser powder bed fusion process. Int J Adv Manuf Technol 110(1–2):191–207. https://doi.org/10.1007/s00170-020-05827-4
28. Williams JL (2001) Monolith structures, materials, properties and uses
29. Moreno-Castilla C, Pérez-Cadenas AF (2010) Carbon-based honeycomb monoliths for environmental gas-phase applications. Materials 3(2):1203–1227. https://doi.org/10.3390/ma3021203
30. Cheng Z, Xu R, Jiang P-X (2021) Morphology, flow and heat transfer in triply periodic minimal surface based porous structures. Int J Heat Mass Transf 170:120902. https://doi.org/10.1016/j.ijheatmasstransfer.2021.120902
31. Busse C, Freund H, Schwieger W (2018) Intensification of heat transfer in catalytic reactors by additively manufactured periodic open cellular structures (POCS). Chem Eng Process Process Intensif 124:199–214. https://doi.org/10.1016/j.cep.2018.01.023
32. Stephan P, Kabelac S, Kind M, Mewes D, Schaber K et al (2019) VDI-Wärmeatlas. Springer, Berlin, p 2019

33. Spurk JH, Aksel N (2020) Fluid mechanics. Springer, Cham, p 590
34. Vhora K, Thévenin D, Janiga G, Sundmacher K (2024) CFD analysis of the flow in Schwarz-D TPMS structures for engineering applications. Chem Ing Tech 96(12):1683–1696. https://doi.org/10.1002/cite.202400093
35. Fand RM, Kim BYK, Lam ACC, Phan RT (1987) Resistance to the flow of fluids through simple and complex porous media whose matrices are composed of randomly packed spheres. J Fluids Eng 109(3):268–273. https://doi.org/10.1115/1.3242658
36. Ou J, Perot B, Rothstein JP (2004) Laminar drag reduction in microchannels using ultrahydrophobic surfaces. Phys Fluids 16(12):4635–4643. https://doi.org/10.1063/1.1812011